Chapter 4
Milling Dynamics

> *If we knew what it was we were doing, it would not be called research, would it?*
>
> –Albert Einstein

In Chapter 3, we applied knowledge of the tool point dynamics from modal analysis (Chapter 2) to predict regenerative chatter in turning using stability lobe diagrams and time-domain simulation. This chapter follows a similar format, but our focus is milling. We again develop force expressions, discuss surface regeneration, and present the relevant equations and examples for stability lobe diagrams. This is followed by a description of time-domain simulation that predict forces and displacements during milling for selected operating parameters. The chapter concludes with a description of the experimental determination of cutting force coefficients.

4.1 Milling Description

In milling, a rotating tool with defined cutting edges is moved relative to a workpiece in order to remove material and obtain the desired workpiece geometry and dimensions. The tool is typically mounted in a holder which is attached to the spindle. The spindle provides the tool's rotational speed, torque, and power. Multiple axes are then used to manipulate the tool-holder-spindle relative to the workpiece. At minimum, three linear axes are generally arranged in a mutually perpendicular configuration; these linear motions are traditionally labeled x, y, and z with the latter indicating the tool axis. However, milling machines are also available with additional rotational axes to provide contouring capabilities for non-prismatic parts. In this case, the rotational degrees of freedom are typically labeled A, B, and C, which indicate rotations about the x, y, and z axes, respectively. As with lathes, milling machines may be manual or computer numerically controlled. Figure 4.1.1 shows an example representation of a three axis milling machine. A vertical spindle configuration is shown, although horizontal spindle geometries are also available. The latter is often

T.L. Schmitz, K.S. Smith, *Machining Dynamics*, DOI 10.1007/978-0-387-09645-2_4,

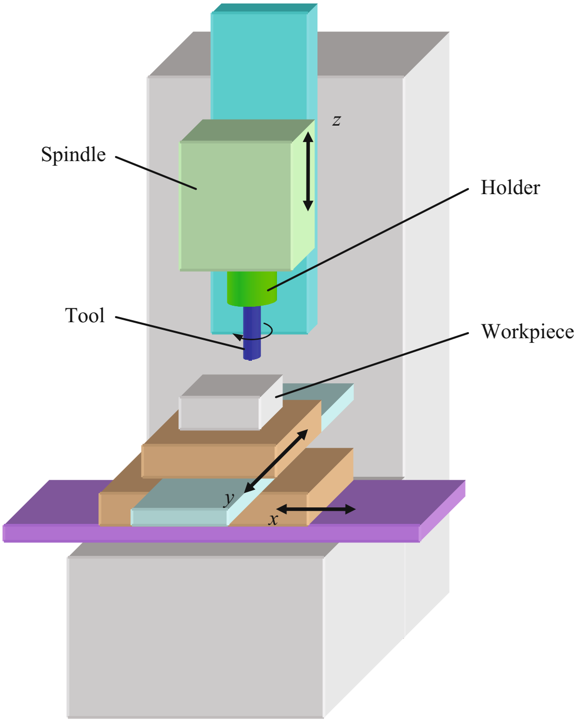

Fig. 4.1.1 Schematic of vertical spindle milling machine. The tool is clamped in a holder which is attached to the rotating spindle. The tool-holder-spindle is moved relative to the workpiece using the three orthogonal axes to remove material in the subtractive milling process

preferred in high speed milling applications because the chips fall from the workpiece for later collection.

Cutting tools and holders are available in many varieties that are tailored to specific applications, such as peripheral, end, contour, and face milling. For analysis purposes, we will focus on peripheral and end milling operations, although the concepts can be extended to other operations as well. Endmills may be loosely categorized according to their free end geometry, including square, ball nose, and bull nose. Square endmills have a cylindrical shape with a small end radius so that the profile is rectangular. Ball nose endmills are hemispherical at their free end to enable contouring of internal cavities and external, three dimensional non-prismatic features. Endmills with a bull nose geometry have larger end radii than square endmills, but are not fully hemispherical. Similar to ball nose endmills, they also allow contouring. See Fig. 4.1.2.

Endmills may have the cutting teeth ground directly into the body or may have replaceable inserts clamped to a cylinder. Typical materials for ground cutters include high speed steel and sintered carbide, while inserted cutters

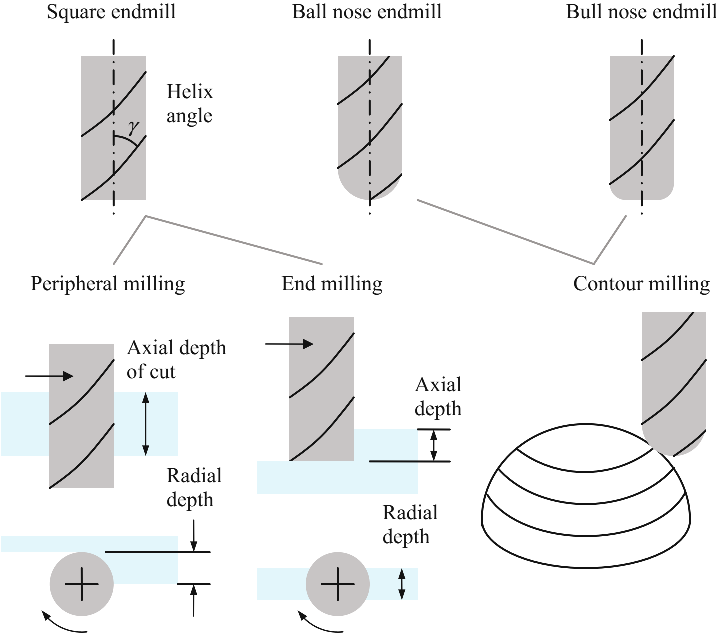

Fig. 4.1.2 Example milling applications and tool geometries.

traditionally use steel bodies with carbide or ceramic inserts. Coatings designed to improve tool life are also often applied in single or multiple layers. For either ground or solid body endmills, the cutting edge is not usually parallel to the tool's rotating axis (referred to as "straight" teeth). Rather, the edge is inclined so that the chip to be removed is spread over an increased length and the cutting edge pressure is reduced. For solid body cutters, the edge is typically ground with a helical profile around the tool periphery using a constant helix angle, γ. The chip width, $\tilde{b}$, is then related to the axial depth of cut, b, as:

$$\tilde{b} = \frac{b}{\cos(\gamma)} \tag{4.1.1}$$

This will have implications for the surface location error calculations described in Chapter 5. However, for now we will neglect the cutting edge's helical shape and assume straight cutter teeth ($\tilde{b} = b$ for $\gamma = 0$). This simplification enables us to obtain some insight into the milling operation and is reasonable if the axial depth of cut is small. A second assumption that we will apply is referred to as the "circular tool path" approximation. The actual path followed by any point on the cutter's periphery as the tool rotates during translation is

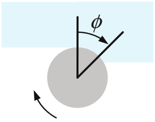

Fig. 4.1.3 Cutter angle definition

cycloidal in nature. However, because the linear advance is generally small relative to the product of the rotational speed and tool radius, the path may be approximated as a series of circles, each offset by the feed per tooth, f_t, so that the time dependent chip thickness can be expressed as:

$$h = f_t \sin(\phi) \tag{4.1.2}$$

where ϕ is the tool's rotational angle; see Fig. 4.1.3. The feed per tooth is described in terms of the linear feed, f, spindle speed, Ω, and number of teeth on the cutter, N_t, in Eq. 4.1.3. Typical units for these variables are mm/tooth for feed per tooth, rpm for spindle speed, mm/min for linear feed rate, and teeth/rev for number of teeth. An improved analytical model for chip thickness is provided in [1], but the circular tooth path approximation offers sufficient accuracy for our purposes.

$$f_t = \frac{f}{\Omega N_t} \tag{4.1.3}$$

As Eq. 4.1.2 shows, the chip thickness in milling varies periodically, even in the absence of tool or workpiece vibrations. It is zero when $\phi = 0$ and 180 deg and maximum (equal to f_t) when $\phi = 90$ deg. Figure 4.1.4 shows this variation for both conventional, or up, and climb, or down, peripheral milling operations. Note that the chip thickness increases during up milling and decreases in down milling. In both cases, it is zero for $180 < \phi < 360$ deg because no cutting occurs between these angles. The entry, or start, angle

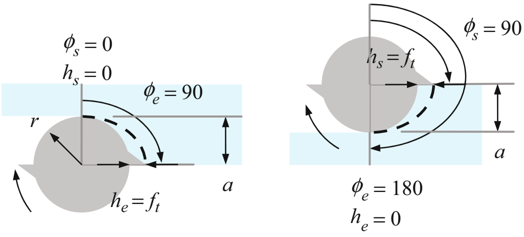

Up milling

Down milling

Fig. 4.1.4 Chip thickness variation for up and down milling ($a = r$)

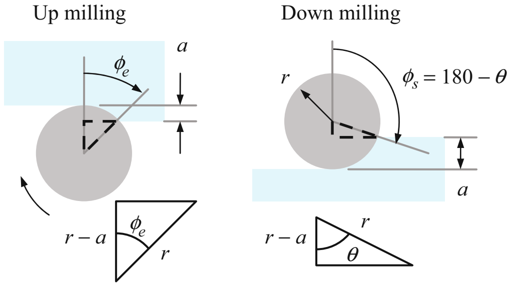

Fig. 4.1.5 Exit and start angle geometry for up and down milling

for up milling is $\phi_s = 0$, while the exit angle, ϕ_e, depends on the radial depth of cut, a, and tool radius, r:

$$\phi_e = \cos^{-1}\left(\frac{r-a}{r}\right) \tag{4.1.4}$$

In down milling, the exit angle is $\phi_e = 180$ deg. Similar to up milling, the start angle is written as a function of the radial depth and tool radius. See Eq. 4.1.5 and Fig. 4.1.5.

$$\phi_s = 180 - \theta = 180 - \cos^{-1}\left(\frac{r-a}{r}\right) \text{ (deg)} \tag{4.1.5}$$

IN A NUTSHELL Whereas in turning operations the chip thickness and chip width are fixed, this is not the case in milling. In a straight slotting cut, the chip thickness encountered by each tooth varies continuously as that tooth enters and exits the cut. In pocket milling, the radial depth of cut may also change. Finally, in sculptured surface milling, the axial depth of cut may vary as well.

Example 4.1.1: Start and exit angles for up milling Consider the peripheral up milling cut shown in Fig. 4.1.6 where the radial depth of cut is 1.9 mm. For a 19 mm diameter (9.5 mm radius) cutter, we will refer to this as a 10% radial immersion cut. (Using this notation, a slotting cut with a radial depth of 19 mm

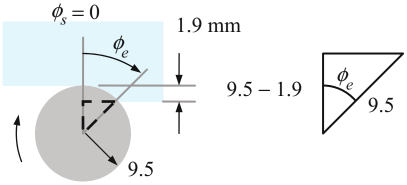

Fig. 4.1.6 Exit angle for 10% radial immersion up milling cut

would be described as 100% radial immersion for the 19 mm diameter cutter.) Because it is an up milling cut, the start angle is $\phi_s = 0$. The exit angle is:

$$\phi_e = \cos^{-1}\left(\frac{9.5 - 1.9}{9.5}\right) = \cos^{-1}(0.8) = 37 \text{ deg}$$

and the instantaneous chip thickness between the start and exit angles can be defined by Eq. 4.1.2.

As with turning, let's begin our discussion of cutting force by assuming a rigid tool and workpiece; that is, by considering the geometry alone. Unlike turning, however, the cutting force is not constant under these conditions. Rather, it is a function of the cutting angle. As we'll see, the cutting force expression is complicated by the chip thickness variation with cutter angle, the number of teeth simultaneously engaged in the cut at any instant, and the projection of the cutting force into a non-rotating coordinate frame. Similar to Eqs. 3.1.1–3.1.3, we can express the cutting force on any cutting edge as a function of the chip area and specific force:

$$F = K_s A = K_s bh. \tag{4.1.6}$$

The normal and tangential components can be written using Eqs. 4.1.7 and 4.1.8, as demonstrated in Fig. 4.1.7:

$$F_n = \cos(\beta)F = \cos(\beta)K_s bh = k_n bh \text{ and} \tag{4.1.7}$$

$$F_t = \sin(\beta)F = \sin(\beta)K_s bh = k_t bh. \tag{4.1.8}$$

This figure shows the cutting force exerted on a single tooth, where the force is described in a coordinate frame that rotates with the tool. For measurement purposes, however, it is generally more convenient to express the force in a fixed frame. For example, the workpiece may be mounted on a cutting force dynamometer and the x, y, and z direction force components recorded during milling (Fig. 4.1.8). To describe these forces analytically, we must project the normal and tangential components into the x and y directions using the cutter angle ϕ. Based on our assumption of straight cutter teeth, we may neglect the z direction component.

$$F_x = F_t\cos(\phi) + F_n\sin(\phi) \tag{4.1.9}$$

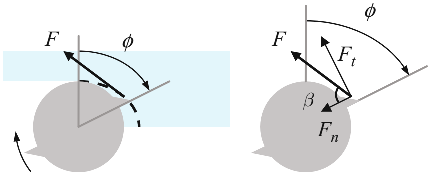

Fig. 4.1.7 Cutting force geometry for milling

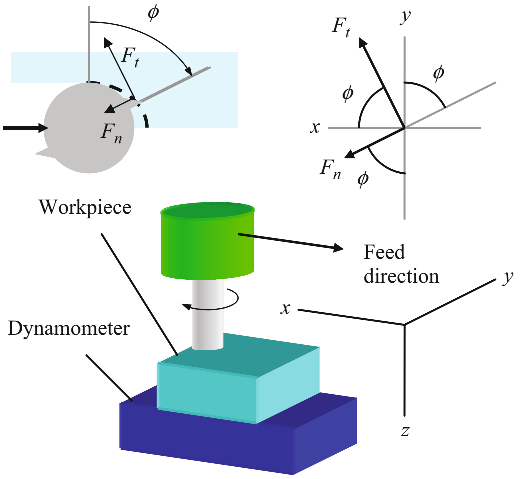

Fig. 4.1.8 Projection geometry for tangential and normal cutting force components into x and y directions.

$$F_y = F_t \sin(\phi) - F_n \cos(\phi) \tag{4.1.10}$$

We can now substitute for the tangential and normal force components in Eqs. 4.1.9 and 4.1.10. This yields:

$$F_x = k_t b f_t \sin(\phi)\cos(\phi) + k_n b f_t \sin(\phi)\sin(\phi) \text{ and} \tag{4.1.11}$$

$$F_y = k_t b f_t \sin(\phi)\sin(\phi) - k_n b f_t \sin(\phi)\cos(\phi), \tag{4.1.12}$$

where we have also replaced the instantaneous chip thickness with the expression provided in Eq. 4.1.2. These forces are clearly periodic with ϕ, but we must also consider the cut geometry in the final force calculations. See the following example.

IN A NUTSHELL As the tool rotates, the force on each tooth changes. In addition, the force orientation (direction) on that tooth varies during the tool rotation. Therefore, the forces generated by a single tooth, as seen by the workpiece or machine tool, vary periodically with the rotation of the tool. In addition, the total force changes as additional teeth enter or leave the cut.

Example 4.1.2: Cutting forces for rigid tool and workpiece Consider a 25% radial immersion peripheral up milling operation carried out using a tool with

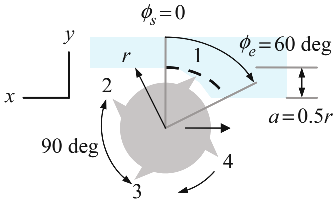

Fig. 4.1.9 25% radial immersion up milling cutting forces for Ex. 4.1.2

four teeth; see Fig. 4.1.9. The radial depth of cut is 25% of the cutter diameter or one half of its radius, $a = \frac{r}{2}$. Because it is an up milling operation, $\phi_s = 0$ and the exit angle is:

$$\phi_e = \cos^{-1}\left(\frac{r - \frac{r}{2}}{r}\right) = \cos^{-1}(0.5) = 60\,\text{deg}.$$

Therefore, each of the four teeth, equally spaced at 90 deg intervals around the periphery of the cutter, is engaged in the cut for only 60 deg. For this 60 deg range, the force components in the fixed x-y frame can be described using Eqs. 4.1.11 and 4.1.12. For the remaining 30 degrees, the forces are zero. The x and y direction cutting forces over one revolution are shown in Fig. 4.1.10, where the resultant force, $F = \sqrt{F_x^2 + F_y^2}$, is also included. For illustration purposes, the following parameters were selected: $k_t = 750$ N/mm^2 and $k_n = 250$ N/mm^2 (corresponds to $K_s = 791$ N/mm^2 and $\beta = 71.6$ deg – these values would be reasonable for an aluminum alloy), $b = 5$ mm, and $f_t = 0.1$ mm/tooth. We see that tooth 1 is engaged between 0 and 60 deg (assuming a start angle of $\phi = 0$ when tooth 1 is vertical). Because the chip thickness increases as the cutter angle

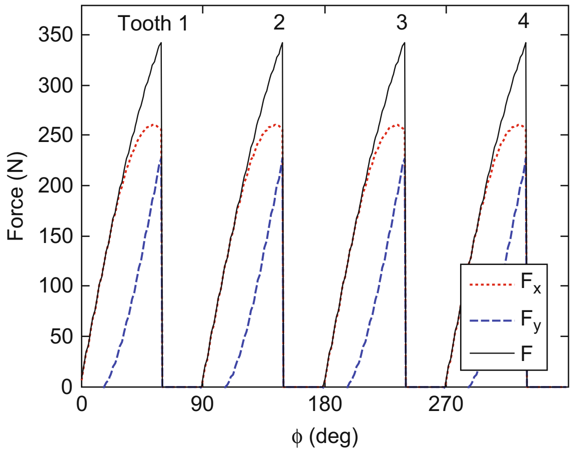

Fig. 4.1.10 25% radial immersion up milling cutting forces for Ex. 4.1.2

increases in up milling, the force levels grow. At 60 deg, the forces drop to zero until tooth 2 enters the cut at $\phi = 90$ deg. It is engaged until 150 deg (60 deg beyond 90 deg) when the force again drops to zero and so on for one full revolution (all four teeth). The MATLAB® program used to produce Fig. 4.1.10 is provided on the companion CD as p_4_1_2_1.m. A detailed description of the code is given in Section 4.4.

For comparison purposes, Fig. 4.1.11 shows the geometry for a 25% radial immersion down milling cut and Fig. 4.1.12 displays the corresponding single revolution cutting force profile. All parameters remain the same, except that the starting angle is:

$$\phi_s = 180 - \cos^{-1}\left(\frac{r - \frac{r}{2}}{r}\right) = 180 - \cos^{-1}(0.5) = 120\,\text{deg}$$

and the exit angle is $\phi_e = 180$ deg. It is observed that tooth 4 enters the cut first (again assuming a start angle of $\phi = 0$ when tooth 1 is vertical). This entry occurs after a 30 deg delay where no cutting occurs (i.e., the 90 deg lead of tooth 4

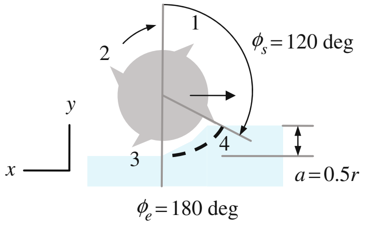

Fig. 4.1.11 25% radial immersion down milling geometry for Ex. 4.1.2

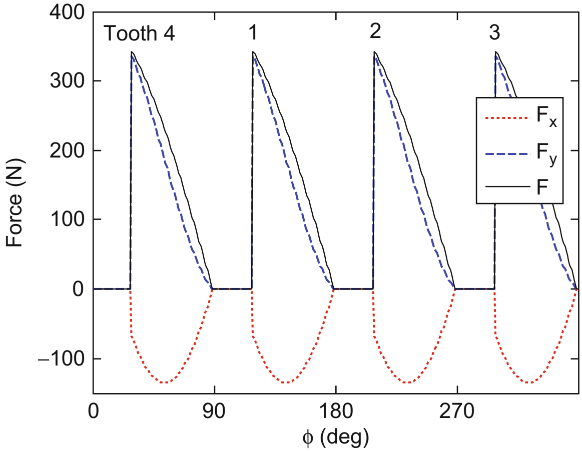

Fig. 4.1.12 25% radial immersion down milling cutting forces for Ex. 4.1.2

relative to tooth 1 plus 30 deg gives the 120 deg cut starting angle). The maximum force level is encountered at 30 deg and then decreases with the chip thickness to an angle of 90 deg; this trend of force reduction as the final surface is being created explains why down milling is often selected for finishing passes when surface finish is most critical. After $\phi = 90$ deg is reached, the force is again zero until tooth 1 enters the cut at 120 deg and the cycle is repeated. Note that the x direction force is now negative (acting to the right). This is in direct contrast to the positive up milling x force seen in Fig. 4.1.10. The MATLAB® program used to produce Fig. 4.1.12 is provided on the companion CD as p_4_1_2_2.m.

4.1.1 Tooth Passing Frequency

As a final point of emphasis for this example, let's discuss the frequency content of cutting force signals. As seen in Figs. 4.1.10 and 4.1.12, the forces during these partial immersion (up and down milling) cuts resemble trains of periodic impulses. To determine the resulting frequency spectrum, we first convert the abscissa to time (s), rather than tooth angle (deg). This conversion requires that the spindle speed, Ω, (rpm) is specified:

$$t = \frac{\phi \cdot 60}{\Omega \cdot 360}\,(\mathrm{s}). \tag{4.1.13}$$

Figures 4.1.13 (up milling) and 4.1.14 (down milling) show the resulting time vs. force plots for a spindle speed of 7500 rpm. It is seen that each tooth passage (90 deg angular interval for the cutter with four teeth) requires 0.002 s, or 2×10^{-3}s. The Fourier transform may now be applied to determine the

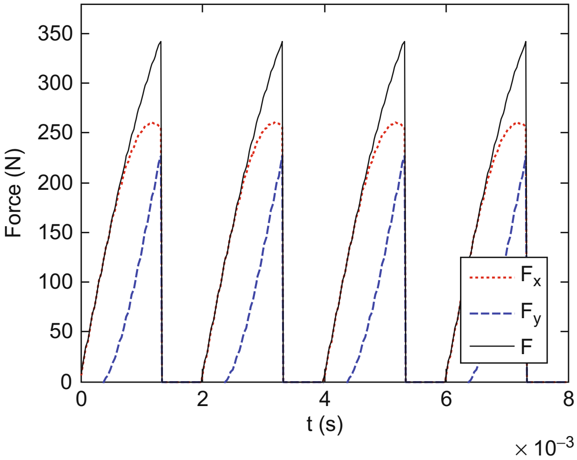

Fig. 4.1.13 Time-domain 25% radial immersion up milling cutting forces for Ex. 4.1.2

frequency content. Because the time-domain signal is a succession of impulse-like peaks, frequency content is observed not only at the tooth passing frequency:

$$f_{tooth} = \frac{\Omega \cdot N_t}{60} \text{(Hz)}, \tag{4.1.14}$$

where the spindle speed is again expressed in rpm, but also at integer multiples of f_{tooth}. We refer to f_{tooth} as the fundamental tooth passing frequency or first harmonic, $2f_{tooth}$ as the second harmonic, and so on. The relative magnitudes of these harmonics depend on the "sharpness" of the force impulses; sharper peaks lead to increased magnitudes of higher order harmonics. Zero frequency, or DC, content is also typically observed. For example, the perfectly sinusoidal x direction force profile obtained for a two tooth cutter in a slotting cut exhibits content at only DC (because its average value is nonzero) and the fundamental tooth passing frequency (because it is a pure sinusoid and not impulsive in nature). Returning to Figs. 4.1.13 and 4.1.14, we saw that the tooth period was 0.002 s. This corresponds to a frequency of $\frac{1}{0.002} = 500$ Hz, which matches the result obtained from Eq. 4.1.14, $f_{tooth} = \frac{7500 \cdot 4}{60} = 500$ Hz. The magnitude vs. frequency plot for the down milling resultant force, F, is shown in Fig. 4.1.15. As expected, peaks are observed at 500 Hz, 1000 Hz, 1500 Hz, and higher order harmonics. This figure was generated using the MATLAB® program p_4_1_2_3.m included on the companion CD. The MATLAB® function `fft` was implemented to compute the fast Fourier transform of the force data.

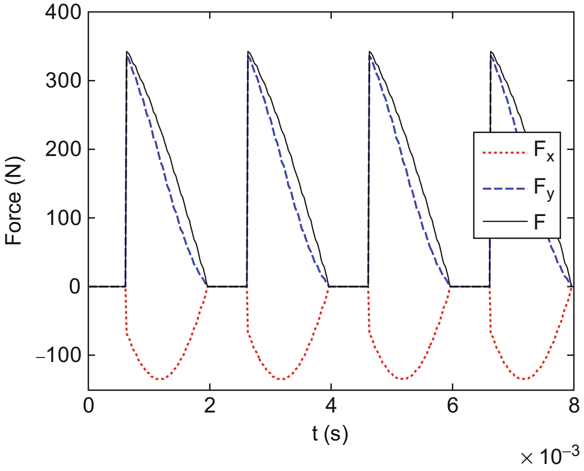

Fig. 4.1.14 Time-domain 25% radial immersion down milling cutting forces for Ex. 4.1.2

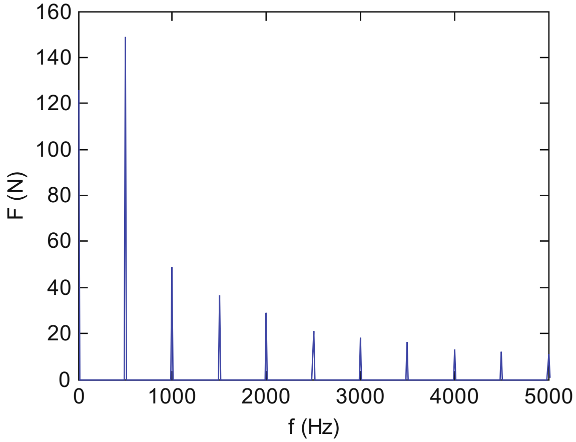

Fig. 4.1.15 25% radial immersion down milling frequency spectrum for resultant force in Ex. 4.1.2

IN A NUTSHELL The cutting force varies with the angle of the cutting edge. By including the spindle speed, we see that the cutting force varies in time and that the forces generated by the teeth are an external excitation that cause forced vibration. Changing the spindle speed modifies the excitation frequency. Because the force is periodic, but not purely sinusoidal, it can be thought of as a combination of many sinusoidal forces and these can be determined using the mathematical technique of the Fourier transform. The resulting plot shows the "frequency content" of the force. In many ways it is like looking at a graphic equalizer in a home stereo system[1] with the height of the peaks in the graph representing the force level at the corresponding frequency.

4.1.2 Multiple Teeth in the Cut

A natural extension of the previous example is to consider cases where there are more teeth on the cutter or the radial immersion is increased. In these instances, it is possible for more than one tooth to be engaged in the cut at a given time. Further, it is possible to alternate between, for example, one tooth cutting

---

[1] The "old" authors realize that graphic equalizer displays on stereos are not as common as they were in our teenage years. For that matter, they don't call them "boom boxes" any more, do they?

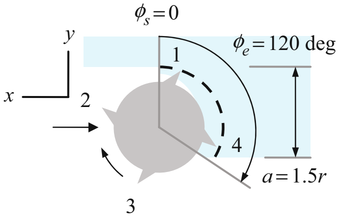

Fig. 4.1.16 75% radial immersion milling geometry

over some interval and two teeth in another. This situation is illustrated in Fig. 4.1.16, where the radial immersion is 75% and the cutter again has four teeth. First, we notice that the cut includes both up ($0 \leq \phi \leq 90$ deg) and down ($90 < \phi \leq 120$ deg) milling portions. Next, we see that when $0 \leq \phi \leq 30$ deg, both teeth 4 and 1 are cutting (assume $\phi = 0$ when tooth 1 is vertical). However, when $30 < \phi \leq 90$ deg, only tooth 1 is engaged. For $90 < \phi \leq 120$ deg, two teeth (1 and 2) are again cutting simultaneously. As ϕ continues to increase, the cycle continues and, unlike the previous example, the cutting force components never drop to zero. As seen in Fig. 4.1.17, during the intervals when two teeth are engaged simultaneously, the cutting forces are constant. This surprising result leads to constant cutting forces at all times for slotting operations with an even number of teeth, where $N_t > 2$. The MATLAB® program p_4_1_2_3.m can be modified to: 1) produce Fig. 4.1.17 by selecting `phie = 120`; and 2) demonstrate the constant force for slotting with $N_t = 4, 6, 8, \ldots$ by setting `phis = 0`, `phie = 180`, and `Nt` to the appropriate value. Because multiple teeth can be cutting at any instant, the force expressions in Eqs. 11 and 12 should be updated to include the necessary summations:

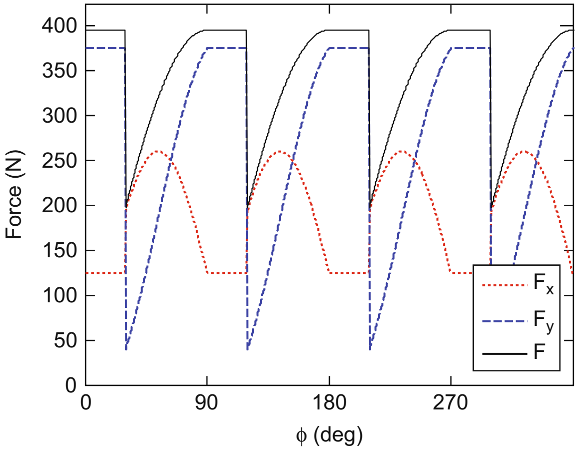

Fig. 4.1.17 75% radial immersion cutting forces

$$F_x = \sum_{j=1}^{N_t} k_t b f_t \sin(\phi_j)\cos(\phi_j) + k_n b f_t \sin(\phi_j)\sin(\phi_j) \text{ and} \tag{4.1.15}$$

$$F_y = \sum_{j=1}^{N_t} k_t b f_t \sin(\phi_j)\sin(\phi_j) - k_n b f_t \sin(\phi_j)\cos(\phi_j), \tag{4.1.16}$$

where ϕ_j is the angle of each tooth on the cutter. For a cutter with four teeth, as shown in Fig. 4.1.9 for example, if the angle for tooth 1 is $\phi_1 = 40$ deg, then the remaining angles are $\phi_2 = 310$ deg, $\phi_3 = 220$ deg, and $\phi_4 = 130$ deg. In this case, each successive tooth angle is decremented by 90 deg (the tooth pitch for equally spaced teeth is equal to 360 deg divided by the number of teeth), where $0 \leq \phi_j < 360$. As we've seen, to calculate the final cutting force we must also verify that the j^{th} tooth in question is between ϕ_s and ϕ_e prior to summing its contribution to the overall force value. Otherwise, the tooth is not engaged in the cut and zero force is added to the summation at that instant.

FOR INSTANCE If the radial depth of cut is very small, there are long periods of time when no tooth is cutting at all. In this case, the cutting force looks like a series of very short impacts. If the radial depth of cut is larger, then the number of teeth cutting simultaneously may be constant or vary depending on the cut geometry and the tooth spacing.

Prior to beginning our discussion of regenerative chatter, let's identify four other important terms related to milling performance.

1. The cutting speed, v, is the peripheral velocity of the cutter and is described by:

$$v = \frac{r\Omega \cdot 2\pi}{60} = \frac{d\Omega \cdot \pi}{60}\,(\text{mm/s}), \tag{4.1.17}$$

where Ω is given in rpm and the tool radius (or diameter) is stated in mm. This quantity is important because the cutting temperature generally increases with cutting speed. Since diffusive tool wear (typically characterized by diffusion of the tool material into the workpiece/chip) is temperature dependent, high temperatures at the tool-chip interface can lead to prohibitive wear and, therefore, place an upper bound on the allowable cutting speed. This, in turn, limits the top available spindle speed (for a given tool diameter) and can reduce the availability of the large stable zones observed to the right of stability lobe diagrams at higher spindle speeds. High temperatures are particularly problematic when the workpiece material exhibits low thermal conductivity. This causes the heat to remain at the tool-chip interface, rather than being conducted away into the workpiece, and accelerates diffusive wear. A well-known example is the difficulty in machining the titanium alloy 6Al-4V, with a thermal conductivity value approximately 20 times less than 7075 aluminum for instance, due to the associated excessive wear rates at high cutting speeds.

2. For any cut to be carried out, the spindle must possess the required torque to continue rotating the tool against the retarding tangential component of the cutting force. The instantaneous torque, T, is expressed as the sum of the products of the tool radius and tangential force for each tooth engaged in the cut. Similar to Eqs. 4.1.15 and 4.1.16, the torque can be written as:

$$T = \sum_{j=1}^{N_t} r \cdot F_{t,j} = r \sum_{j=1}^{N_t} F_{t,j} = r \sum_{j=1}^{N_t} k_t b f_t \sin(\phi_j) = r k_t b f_t \sum_{j=1}^{N_t} \sin(\phi_j), \tag{4.1.18}$$

   where the same ϕ_j definition holds and typical units for torque are N-m. For most spindles, the available torque is spindle speed dependent and is provided as a "torque curve" with the spindle specifications. Because the rotating spindle has inertia, it acts like a flywheel. For that reason it is often the average torque, rather than the instantaneous torque, that matters. The cutting operation can briefly sustain a torque in excess of the torque curve (thereby slightly slowing the rotation of the spindle) if the average torque is sufficiently low.

3. Similar to torque, the available spindle power can limit the potential cut geometry (i.e., if the power is exceeded, the spindle will stall). The power is determined from the product of torque and rotational speed. If the spindle speed is expressed in rpm and torque in N-m, the power in W is:

$$P = \frac{T\Omega \cdot 2\pi}{60}. \tag{4.1.19}$$

   Again, the spindle power is a function of spindle speed and is expressed via a "power curve" supplied by the spindle manufacturer. Like torque, it is often the average power that counts. Interestingly, the average power is proportional to the average metal removal rate.

4. In order to reduce machining time and, subsequently, cost, it is often desired to increase the mean material removal rate, MRR, or average volume of material removed per unit time.

$$MRR = abf = abf_t N_t \Omega \tag{4.1.20}$$

4.2 Regenerative Chatter in Milling

If we remove the assumption of a rigid tool, then the cutting force could cause deflections of the tool[2]. Additionally, if the tool is vibrating as it removes material, we would expect these vibrations to be "imprinted" on the workpiece

---

[2] We will assume a rigid workpiece in our analysis.

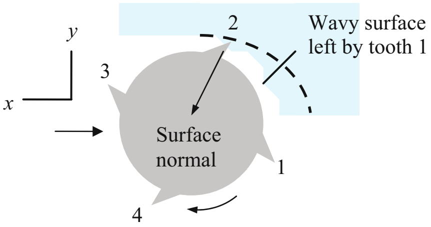

Fig. 4.2.1 Regeneration in milling. Cutter deflections during the passage of tooth 1 are copied onto the workpiece surface and are encountered by tooth 2. This varies the chip thickness and cutting force which, in turn, affects the resulting tool deflections

surface as a wavy profile just as we discussed for turning. The difference in milling is that the time-delayed surface regeneration step occurs from tooth to tooth, rather than from revolution to revolution as in turning. Figure 4.2.1 shows that the wavy surface left behind by tooth 1 is removed by tooth 2 and so on. This again provides a feedback mechanism because the instantaneous chip thickness depends on both the current vibration and the surface left by the previous tooth (one tooth period, or time from one tooth to the next, earlier). The variable chip thickness governs the cutting force which, in turn, affects subsequent tool vibrations. The result is the possibility for instability, or chatter, just as we saw with turning operations. We will again consider vibrations normal to the cut surface in order to determine the chip thickness. However, this normal direction (through the cutting edge toward the tool center) constantly varies as the cutter rotates; see Fig. 4.2.1.

Analogous to turning, the relative phasing between the surface waviness from one tooth to the next determines the level of force variation and, together with the chip width, whether the operation is stable or unstable. Figures 4.2.2 and 4.2.3 show two possibilities. In Fig. 4.2.2, the wavy surface and current vibration between two subsequent teeth are in phase. Therefore, even though the tool is vibrating during material removal, the chip thickness variation (along the instantaneous surface normal) is similar to what would be obtained from the cycloidal tool path alone. This tends to produce forced vibration only and

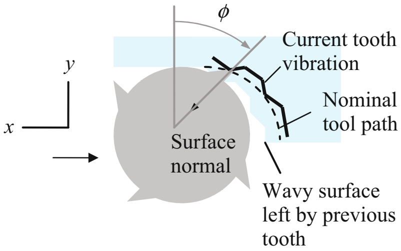

Fig. 4.2.2 Condition when the vibrations from one tooth to the next are in phase. This yields chip thickness variation that seen for the cycloidal tool path only

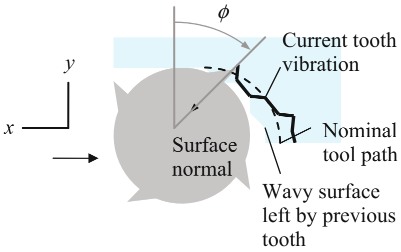

Fig. 4.2.3 Out of phase condition where the tool vibrations from one tooth to the next lead to significant chip thickness variation

stable cutting. Again, because the tool vibrates at its natural frequency (we'll assume a single degree of freedom system for now), it is intuitive that matching the tooth passing frequency to the tool's natural frequency will lead to this preferred "in phase" situation. We recognize, however, that driving the system at resonance does lead to larger vibration levels, although much less than what would be obtained during chatter. We will explore this issue further in Chapter 5. Figure 4.2.3 shows a less favorable phase relationship where there is significant variation in the chip thickness (beyond the periodic variation due to the cycloidal tool path). This can lead to self-excited vibrations and unstable cutting, depending on the chip width, due to the force variations and subsequent tool deflections.

IN A NUTSHELL Although the geometry is more complicated, milling stability is conceptually similar to turning. The varying cutting force causes vibration of the tool, which generates a wavy surface. The wavy surface causes a variable chip thickness which, in turn, yields a variable cutting force. Depending on the cutting conditions and the alignment of the waves, the vibration can grow (chatter) or diminish (stable) with subsequent tooth passes.

As mentioned, the chip thickness is measured along the surface normal just as for turning, but the surface normal is a function of the cutter angle ϕ. The projection of the instantaneous chip thickness along the surface normal under the circular tool path assumption is characterized by Eq. 4.1.2 in the absence of tool vibrations. However, if we now allow the tool to undergo vibrations in the x and y directions due to the application of the cutting force to the non-rigid tool, the chip thickness equation must be modified. First, we can project the x and y vibrations onto the surface normal, n, according to:

$$n = x\sin(\phi) - y\cos(\phi). \tag{4.2.1}$$

Note that the positive direction for n is out of the cut. Because ϕ varies with time, $\phi = \Omega \cdot 2\pi \frac{180}{\pi} \frac{1}{60} t = 6 \cdot \Omega t \mathrm{deg}$ where Ω is given in rpm and t in s, the direction of n is also a function of time. Similar to the chip thickness in turning, Eq. 3.2.1, the instantaneous chip thickness for milling can then be written as:

$$h(t) = f_t \sin(\phi) + n(t - \tau) - n(t), \tag{4.2.2}$$

where $f_t \sin(\phi)$ replaces the "mean chip thickness" in Eq. 3.2.1 and τ is the tooth period in seconds. The $n(t-\tau)$ term represents the vibration contributions along the surface normal by the previous tooth and $\tau = \frac{60}{\Omega N_t}$ (this is the reciprocal of Eq. 4.1.14), where Ω is again given in rpm. The geometry of Eq. 4.2.2 is shown in Fig. 4.2.4. As we saw in turning, larger (more positive) vibrations by the previous tooth increase the chip thickness because less material is removed than commanded. Larger vibrations by the current tooth lead to decreased chip thickness by the same logic. If the vibrations from one tooth to the next are equal, Eq. 4.2.2 reduces to Eq. 4.1.2. To complete our analogy to turning, let's "unwrap" the milled surface and show the current and previous vibrations along the "planar" instantaneous surface normal. We can observe the similarity of Fig. 4.2.5 for milling to Fig. 4.2.4 for turning. The inherent chip thickness variation due to the cycloidal tool path is schematically represented as a wedge (an up milling cut is presumed where the chip thickness grows as the cutter rotates). In Fig. 4.2.5, recall that v is the cutting speed; its direction is shown.

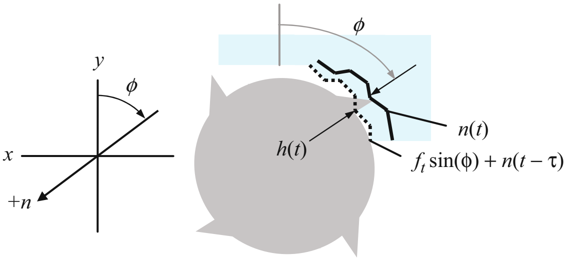

Fig. 4.2.4 Geometry of instantaneous chip thickness calculation for milling

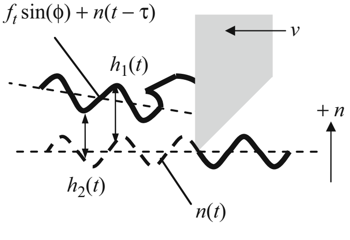

Fig. 4.2.5 Unwrapped view of milled surface for comparison to chip thickness variation in turning

4.3 Stability Lobe Diagrams

4.3.1 Average Tooth Angle Approach

Tlusty modified his turning analysis, presented in Section 3.3, to accommodate the milling process [2–4]. A primary obstacle to defining an analytical solution to milling stability (aside from the inherent time delay) is the time dependence of the cutting force direction. Tlusty solved this problem by assuming an "average" angle of the tooth in the cut and, therefore, an average force direction. This created an autonomous, or time invariant, system. He then made use of directional orientation factors to first project this force into the x and y mode directions and, second, project these results onto the surface normal. Just as for turning, depending on the feedback system "gain", represented by the chip width, b, and the spindle speed, Ω, the milling operation is either stable or it exhibits chatter. Let's first discuss the required equations and then determine the directional orientation factors for various radial immersions.

$$b_{\lim} = \frac{-1}{2K_s \mathrm{Re}[FRF_{orient}]N_t^*}. \tag{4.3.1}$$

$$\frac{f_c}{\Omega N_t} = N + \frac{\varepsilon}{2\pi} \tag{4.3.2}$$

$$\varepsilon = 2\pi - 2\tan^{-1}\left(\frac{\mathrm{Re}[FRF_{orient}]}{\mathrm{Im}[FRF_{orient}]}\right) \tag{4.3.3}$$

Due to the assumption of a fixed force direction, only minor modifications are necessary to adapt the turning stability equations to the milling case. In Eq. 4.3.1, a new variable, N_t^*, appears in the denominator. This represents the average number of teeth in the cut. As discussed in Section 4.1, it is possible for multiple teeth to be engaged simultaneously and, further, for the number of teeth in the cut to vary over one revolution. This average value is calculated by dividing the difference between the exit and starting angles by the angular tooth spacing (we'll assume equal, or proportional, teeth spacing for now). See Eq. 4.3.4, where the start and exit angles are given in deg. We also see that Eq. 4.3.2 differs from Eq. 3.3.2 by a single term. Specifically, N_t appears in the denominator of the left hand side. Because the product ΩN_t represents the tooth passing frequency, the left hand side gives the ratio of the chatter frequency to the forcing frequency. (Units compatibility requires that Ω is given in rev/s if f_c is expressed in Hz.) This is analogous to Eq. 3.3.2, where the ratio is $\frac{f_c}{\Omega}$ because the forcing frequency is simply the rotating speed in turning.

$$N_t^* = \frac{\phi_e - \phi_s}{\frac{360}{N_t}}. \tag{4.3.4}$$

The milling stability lobe diagram is generated by: 1) determining the oriented FRF and identifying the valid chatter frequency range(s), i.e., where the real part is negative; 2) solving for ε; the phase between the current and previous tooth vibrations, over the valid frequency range(s); 3) finding the average number of teeth in the cut for the selected radial immersion; 4) calculating $b_{\lim}$ over the valid frequency range(s); 5) selecting an N value (integer number of waves between teeth) and calculating the associated spindle speeds over the valid frequency range(s); and 6) plotting Ω vs. $b_{\lim}$ (both are a function of the same frequency vector, so the first spindle speed value corresponds to the first limiting chip width and so on) for each N value ($N = 0, 1, 2, \ldots$). Just as with turning, any (Ω, $b_{\lim}$) pair that appears above the collective boundary indicates unstable behavior, while any pair below the boundary indicates stable cutting. Notice that because the N value denotes the integer number of waves between teeth, rather than the integer number of waves per revolution as in turning, the expanded stable zones appear at much lowers spindle speeds. For this reason, the use of the stability lobe diagram to find high performance stable zones in milling is a much more enticing prospect than it is in turning.

4.3.2 Oriented FRF

The oriented FRF is calculated by summing the products of the directional orientation factors and corresponding FRFs for the x and y directions; see Eq. 4.3.5. We'll show the directional orientation factor computations through examples.

$$FRF_{orient} = \mu_x FRF_x + \mu_y FRF_y \tag{4.3.5}$$

Example 4.3.1: Directional orientation factors for slotting For a 100% radial immersion (slotting) cut, the cut start angle is 0 deg and the exit angle is 180 deg (based on the circular tool path approximation). The average angle of a tooth in the cut is therefore:

$$\phi_{ave} = \frac{\phi_s + \phi_e}{2} = \frac{0 + 180}{2} = 90\,\text{deg}.$$

The surface normal is drawn at ϕ_{ave} with the positive direction out of the cut and the cutting force, F, is oriented at the force angle, β, (opposing the direction of rotation) with respect to the surface normal. Figure 4.3.1 shows this geometry.

Two steps are required to determine the x and y direction directional orientation factors. First, the force is projected onto the mode direction. Second, this result is projected onto the surface normal. These two steps are repeated once for each direction. For μ_x, projection onto the x direction gives $F_x = F\cos(\beta)$. The projection of this result onto the "average" surface normal is:

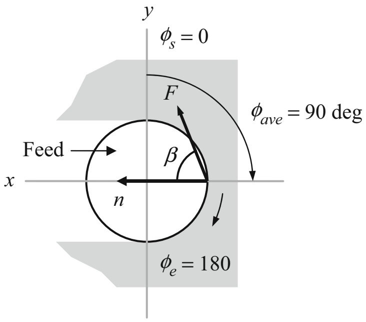

Fig. 4.3.1 Geometry for determining slotting directional orientation factors

$$F_n = F_x \cos(0) = F\cos(\beta)\cos(0) = F\cos(\beta)$$

because the surface normal is parallel to the mode direction in this instance. The directional orientation factor is then $\mu_x = \cos(\beta)$. For μ_y, projection onto the y direction gives $F_y = F\cos(90 - \beta) = F\sin(\beta)$, where β is expressed in deg. The projection of this result onto the "average" surface normal is $F_n = F_y \cos(90) = F\sin(\beta)\cos(90) = 0$ because the surface normal is perpendicular to the mode direction in this instance. The directional orientation factor is then $\mu_y = 0$. According to Eq. 4.3.5, the oriented FRF is $FRF_{orient} = \cos(\beta)FRF_x + 0 \cdot FRF_y$, which suggests that compliance in the y direction has no influence on the milling stability.

Example 4.3.2: Directional orientation factors for down milling Consider the 50% radial immersion down milling cut pictured in Fig. 4.3.2. To find μ_x, we first project F onto the x direction to obtain $F_x = F\cos(45 + \beta)$, where β is given in deg. The projection of this result onto the average surface normal, which occurs at the angle $\phi_{ave} = \frac{90+180}{2} = 135$ deg, is:

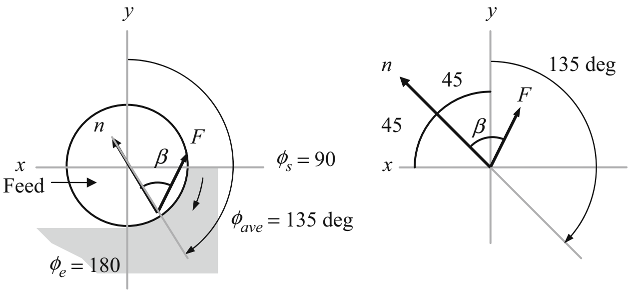

Fig. 4.3.2 Geometry for determining 50% radial immersion down milling directional orientation factors

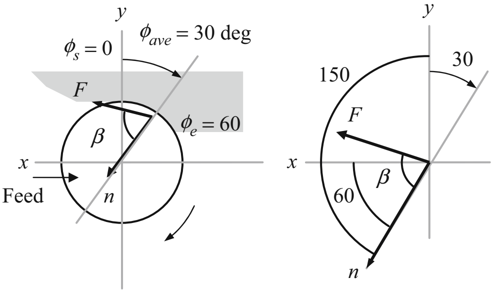

Fig. 4.3.3 Geometry for determining 25% radial immersion up milling directional orientation factors

$$F_n = F_x \cos(45) = F \cos(45 + \beta)\cos(45)$$

For μ_y, projection onto the y direction gives $F_y = F\cos(\beta - 45)$. The projection of this result onto the average surface normal is $F_n = F_y \cos(45) = F\cos(\beta - 45)\cos(45)$. The directional orientation factors are $\mu_x = \cos(45 + \beta)\cos(45)$ and $\mu_y = \cos(\beta - 45)\cos(45)$.

Example 4.3.3: Directional orientation factors for up milling A 25% radial immersion up milling cut in depicted in Fig. 4.3.3. As shown in Eq. 4.1.4, the exit angle is $\phi_e = \cos^{-1}\left(\frac{r-\frac{r}{2}}{r}\right) = \cos^{-1}(0.5) = 60$ deg. The start angle for any up milling cut is zero. To find μ_x, we first project F onto the x direction to obtain $F_x = F\cos(\beta - 60)$, where β is given in deg. The projection of this result onto the average surface normal, which occurs at the angle $\phi_{ave} = \frac{0+60}{2} = 30$ deg, is $F_n = F_x \cos(60) = F\cos(\beta - 60)\cos(60)$. For μ_y, projection onto the y direction gives $F_y = F\cos(150 - \beta)$. The projection of this result onto the average surface normal is $F_n = F_y \cos(150) = F\cos(150 - \beta)\cos(150)$. The directional orientation factors are $\mu_x = \cos(\beta - 60)\cos(60)$ and $\mu_y = \cos(150 - \beta)\cos(150)$.

Let's now examine stability lobes for milling. We'll see that the stability limit is again a mapping of the real part of the oriented FRF onto the (Ω, b_{lim}) diagram. In the following slotting example, we'll demonstrate analytical calculations for the best and worst spindle speeds and $b_{\text{lim,crit}}$ and show the resulting stability lobes. We'll then complete an example for 20% radial immersion down milling.

Example 4.3.4: Slotting stability lobe calculations For this example, the x and y direction dynamics are symmetric and can be described by $f_n = 500$ Hz, $k = 8 \times 10^6$ N/m $= 8 \times 10^3$ N/mm, and $\zeta = 0.02$. As shown in Ex. 4.3.1, the directional orientation factors are $\mu_x = \cos(\beta)$ and $\mu_y = 0$ for slotting and the oriented FRF is $FRF_{orient} = \cos(\beta) FRF_x$. We'll assume an aluminum alloy machined with a four tooth, 19 mm diameter square endmill that together exhibit a specific force of 750 N/mm^2 and a force angle of 68 deg.

For this single degree of freedom example, the best spindle speed is defined for a phase angle of $\varepsilon = 2\pi$ rad $= 360$ deg (see Fig. 3.3.6) just as we observed for turning. The corresponding chatter frequency is $f_c = f_n$. Equation 4.3.2 shows that the best spindle speed for the $N = 0$ lobe is:

$$\Omega_1 = \frac{f_c}{N_t} \cdot \frac{1}{N + \frac{\varepsilon}{2\pi}} = \frac{f_n}{4} \cdot \frac{1}{0 + \frac{2\pi}{2\pi}} = \frac{f_n}{4} = \frac{500}{4} = 125 \text{ rps}$$

or $125 \cdot 60 = 7500$ rpm. This provides a reasonable target spindle speed for milling. Note that for turning (with $N_t = 1$, effectively), the best spindle speed for $N = 0$ is 500 rps or 30000 rpm. Also, the tooth passing frequency for this spindle speed is:

$$f_{tooth} = \frac{\Omega \cdot N_t}{60} = \frac{7500 \cdot 4}{60} = 500\,\text{Hz}$$

Point 1, where f_{tooth} is set equal to f_n, is identified in Fig. 4.3.4. The theoretical limiting chip width for point 1 is:

$$b_1 = \frac{-1}{2K_s \text{Re}[FRF_{orient}]N_t^*} = \frac{-1}{2K_s \cdot 0 \cdot N_t^*} = \infty.$$

However, just as with turning, the $N = 1$ lobe truncates the $N = 0$ lobe and gives a finite chip width where they cross. The average number of teeth in the cut is $N_t^* = \frac{180-0}{\frac{360}{4}} = 2$ for this slotting example.

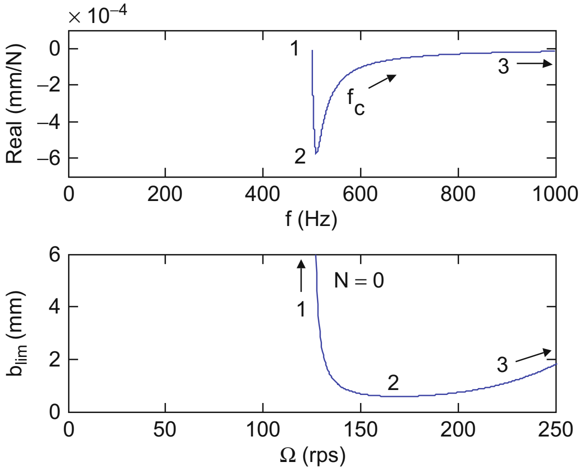

Fig. 4.3.4 Mapping of the oriented FRF onto the (Ω, b_{lim}) diagram for Ex. 4.3.4

The worst spindle speed is obtained when ε is $\frac{3\pi}{2}$ rad or 270 deg (see Fig. 3.3.4). The chatter frequency for this case (i.e., the frequency for min(Re[FRF_{orient}] or min(Re[$\mu_x FRF_x$])) is $f_c = f_n(1+\zeta)$. Substitution in Eq. 4.3.2 gives:

$$\Omega_2 = \frac{f_c}{N_t} \cdot \frac{1}{N + \frac{\varepsilon}{2\pi}} = \frac{f_n(1+\zeta)}{4} \cdot \frac{1}{0 + \frac{\frac{3\pi}{2}}{2\pi}} = \frac{f_n(1+\zeta)}{4} \frac{1}{0 + \frac{3}{4}} = \frac{500(1+0.02)}{3} = 170\,\text{rps}$$

or 10200 rpm. Point 2 is also shown in Fig. 4.3.4. The corresponding minimum limiting chip width, $b_{\text{lim,crit}}$, is determined by rewriting Eq. 4.3.1, $b_{\text{lim,crit}} = \frac{-1}{2K_s \min(\text{Re}[\mu_x FRF_x])N_t^*}$. For a single degree of freedom system, the minimum real part can be approximated by:

$$\min(\text{Re}[FRF]) = \frac{-1}{4k\zeta(1+\zeta)}. \tag{4.3.6}$$

We can therefore write a simple expression for the point 2 chip width (in this single degree of freedom, slotting example):

$$b_{\text{lim,crit}} = \frac{4k\zeta(1+\zeta)}{2K_s \mu_x N_t^*} = \frac{4 \cdot 8 \times 10^3 \cdot 0.02 \cdot (1+0.02)}{2 \cdot 750 \cdot \cos(68) \cdot 2} = 0.58\,\text{mm}$$

Point 3, where $f_c \to \infty$, is similar to point 1 in Fig. 4.3.4. As shown previously in Fig. 3.3.8, even though the tooth to tooth phase relationship is unfavorable ($\varepsilon \to 180$ deg, or exactly out of phase), the response amplitude approaches zero, $\text{Re}(FRF) \to 0$, so the vibration level is small. Substitution in Eq. 4.3.1 yields an infinite chip thickness, $b_3 = \frac{-1}{2K_s \cdot 0 \cdot N_t^*} = \infty$. However, the left end of the $N = 0$ curve, where $f_c = 0$, serves to limit the right hand side of the $N = 1$ curve, where $f_c \to \infty$. Figure 4.3.5 shows the $N = 0$ to 3 lobes for this example. The

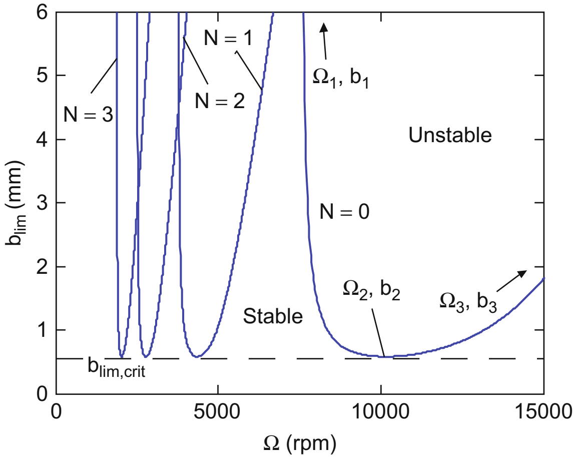

Fig. 4.3.5 Stability lobe diagram for Ex. 4.3.4 ($N = 0$ to 3)

MATLAB® program used to produce Fig. 4.3.5 is provided on the companion CD as p_4_3_4_1.m.

To conclude this example, let's calculate the mean material removal rate if we selected (Ω_2, b_2) with a feed per tooth of 0.15 mm/tooth as the operating parameters. As shown in Eq. 4.1.20, the mean MRR for milling is computed from the product of the axial depth of cut, radial depth (equal to the tool diameter for slotting), feed per tooth, number of teeth, and spindle speed:

$$MRR = b_{\text{lim,crit}} \cdot d \cdot f_t \cdot N_t \cdot \Omega_2 = 0.58 \cdot 19 \cdot 0.15 \cdot 4 \cdot 10200 = 67442\,\text{mm}^3/\text{min}.$$

To visualize this removal rate, let's divide by 60×10^3 to determine the cubic centimeters per second, $MRR = 1.1240\,\text{cm}^3/\text{sec}$. This means that the equivalent of approximately a 1 cm x 1 cm x 1 cm cube of aluminum is removed each second under these conditions.

Example 4.3.5: 20% radial immersion down milling stability lobe calculations Figure 4.3.6 shows the geometry for a 20% radial immersion down milling cut. The start angle is $\phi_s = 180 - \cos^{-1}(0.6) = 126.9$ deg and the exit angle is $\phi_e = 180$ deg. The average angle of a tooth in the cut is $\phi_{ave} = \frac{126.9+180}{2} = 153.4$ deg. The x (feed) direction dynamics are given by $f_{nx} = 900$ Hz, $k_x = 9 \times 10^6$ N/m $= 9 \times 10^3$ N/mm, and $\zeta_x = 0.02$. The y direction dynamics are $f_{ny} = 950$ Hz, $k_y = 1 \times 10^7$ N/m $= 1 \times 10^4$ N/mm, and $\zeta_y = 0.01$. The workpiece material is a low carbon steel alloy and it is machined with a three tooth, 19 mm diameter square endmill. Together they give a specific force of $K_s = 2250$ N/mm^2 and a force angle of $\beta = 75$ deg.

As shown in Fig. 4.3.6, the directional orientation factor for the x direction is determined from the two projections:

$$F_x = F\cos(63.4+\beta)\text{and}F_n = F_x\cos(63.4) = F\cos(63.4+\beta)\cos(63.4),$$

where β is expressed in deg. Therefore, $\mu_x = \cos(63.4+\beta)\cos(63.4) = -0.335$. For the y direction, the projections are:

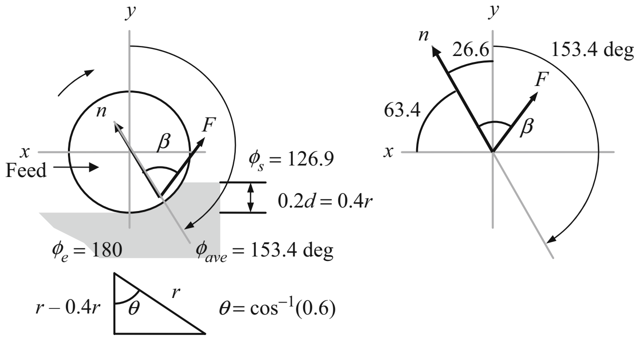

Fig. 4.3.6 Geometry for Ex. 4.3.5 20% radial immersion down milling cut

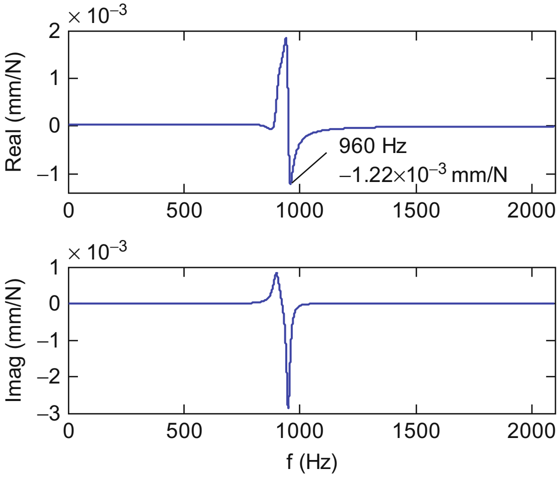

Fig. 4.3.7 Oriented FRF for Ex. 4.3.5

$$F_y = F\cos(\beta - 26.6) \text{ and } F_n = F_y\cos(26.6) = F\cos(\beta - 26.6)\cos(26.6)$$

and $\mu_y = \cos(\beta - 26.6)\cos(26.6) = 0.594$. Additionally, the average number of teeth in the cut is: $N_t^* = \frac{180-126.9}{\frac{360}{3}} = 0.443$.

The oriented FRF is shown in Fig. 4.3.7. The unusual shape of the real and imaginary parts is due to the negative μ_x value. The minimum real part is observed at 960 Hz with a value of -1.22×10^{-3} mm/N. The corresponding worst spindle speed (for the $N = 0$ lobe) and $b_{\text{lim,crit}}$ are approximated by:

$$\Omega_{worst} = \frac{960}{3} \cdot \frac{1}{0 + \frac{\frac{3\pi}{2}}{2\pi}} = \frac{960}{3}\frac{4}{3} = 427\,\text{rps} = 25600\,\text{rpm and}$$

$$b_{\text{lim,crit}} = \frac{-1}{2 \cdot 2250(-1.22 \times 10^{-3})0.443} = 0.41\,\text{mm}$$

The real part of the oriented FRF for the valid chatter frequency ranges ($\text{Re}[FRF_{orient}] < 0$) and the corresponding $N = 0$ stability lobe are shown in Fig. 4.3.8. Two valid ranges are seen; the first, lower frequency range is much stiffer than the second. The "competing lobe" effect of this stiffer section is observed in Fig. 4.3.9, where the $N = 0$ to 4 lobes are plotted. In this case, the stability boundary is nearly completely established by the much more flexible section. The "best speeds" equation from Section 3.3 can also be updated for milling:

$$\Omega_{best} = \frac{f_n \cdot 60}{(N+1) \cdot N_t}(\text{rpm}). \tag{4.3.7}$$

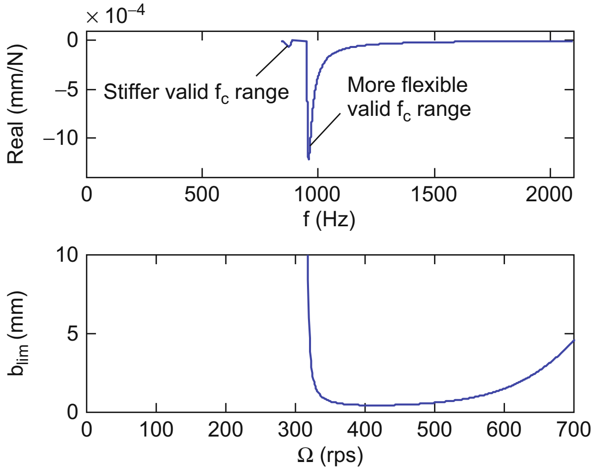

Fig. 4.3.8 (Top) Valid chatter frequency ranges for the real part of the oriented FRF. (Bottom) $N = 0$ stability lobe

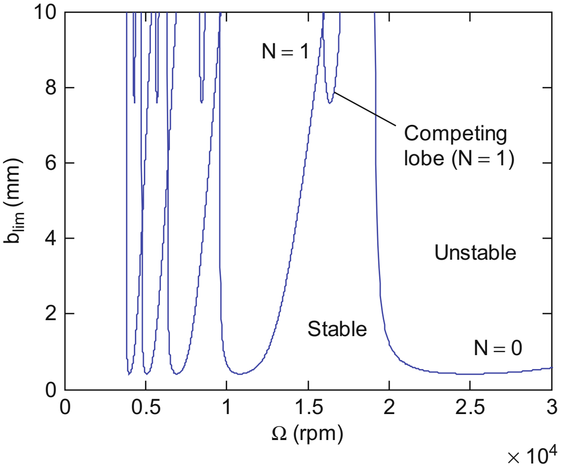

Fig. 4.3.9 Example 4.3.5 stability lobe diagram ($N = 0$ to 4)

If we choose f_n to be the zero crossing for the more flexible real part valid chatter frequency range (at 951 Hz from Figs. 4.3.7 and 4.3.8), then the associated best speeds are 19020 rpm, 9510 rpm, 6340 rpm, and so on for the three tooth endmill. These speeds match those seen in Fig. 4.3.9 for the right hand side of the stable zones moving from right to left on the diagram. For example, 19020 rpm corresponds to the stable gap created by the intersection of the $N = 0$ and $N = 1$ lobes. The MATLAB® program used to produce these figures is provided on the companion CD as p_4_3_5_1.m.

4.3.3 Fourier Series Approach

In [5], Altintas and Budak use an alternate technique to transform the dynamic milling equations into a time invariant, but radial immersion dependent system. Similar to Tlusty, they approximate the time dependent cutting forces by an average value, but employ a different approach to identify this mean. Rather than using the average angle of the tooth in the cut, the time varying coefficients of the dynamic milling equations, which depend on the angular orientation of the tool as it rotates through the cut, are expanded into a Fourier series and then the series is truncated to include only the average component. We'll first present a brief review of this approach and then rearrange the analytical stability equations into the form expected by the MATLAB® `eig` function.

The development of the time dependent cutting force equations closely follows the previous analysis. The primary difference is that the positive x direction is taken to be in the direction of the feed (following the convention in [5]); compare Fig. 4.3.10 (Fourier series) to Fig. 4.1.9 (average tooth angle). The projection of the x and y vibrations onto the surface normal (referred to as the radial direction in [5]) is now:

$$n = -x\sin(\phi) - y\cos(\phi) \tag{4.3.8}$$

and the instantaneous chip thickness equation for tooth j becomes:

$$h(\phi_j) = \left(f_t\sin(\phi_j) + n_{j-1} - n_j\right)\cdot g(\phi_j), \tag{4.3.9}$$

where the switching function, $g(\phi_j)$, is equal to one when the j^{th} tooth is engaged in the cut (i.e., between the cut start and exit angles) and zero otherwise; see Eq. 4.3.10. Also, n_{j-1} indicates the normal direction vibration from the previous tooth and n_j the current tooth vibration.

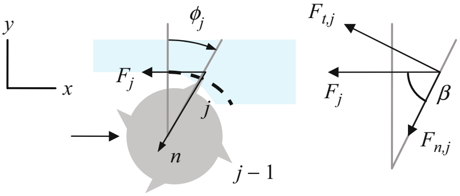

Fig. 4.3.10 Notation for Fourier series stability analysis

$$g(\phi_j)=\left\{\begin{matrix}1, & \text{when} & \phi_s\le\phi_j\le\phi_e\\ 0, & \text{when} & \phi_j<\phi_s,\phi_j>\phi_e\end{matrix}\right\} \tag{4.3.10}$$

If the variable x and y contributions are substituted into Eq. 4.3.9 and the nominal component$f_t\sin(\phi_j)$is neglected (because we are interested in linear stability), the cutter angle dependent chip thickness in the normal direction may be written as shown in Eq. 4.3.11.

$$\begin{aligned}h(\phi_j)&=((-x_{j-1}\sin(\phi_j)-y_{j-1}\cos(\phi_j))-(-x_j\sin(\phi_j)-y_j\cos(\phi_j)))\cdot g(\phi_j)\\ h(\phi_j)&=((x_j-x_{j-1})\sin(\phi_j)+(y_j-y_{j-1})\cos(\phi_j))\cdot g(\phi_j)\\ h(\phi_j)&=(\Delta x\cdot\sin(\phi_j)+\Delta y\cdot\cos(\phi_j))\cdot g(\phi_j)\end{aligned} \tag{4.3.11}$$

The tangential and normal (radial) force components are then written as a function of the chip thickness:

$$F_{t,j}=K_tbh(\phi_j) \text{ and } F_{n,j}=K_nF_{t,j}=K_nK_tbh(\phi_j), \tag{4.3.12}$$

where K_t is equal to the previously defined tangential specific force k_t. The relationship between (K_t, K_n) and K_s is defined using Fig. 4.3.10:

$$F_j=K_sbh(\phi_j) \quad F_j=\sqrt{F_{t,j}^2+F_{n,j}^2}=\sqrt{K_t^2+K_n^2K_t^2}bh(\phi_j)=K_t\sqrt{1+K_n^2}bh(\phi_j), \tag{4.3.13}$$

so that $K_s=K_t\sqrt{1+K_n^2}$. Also, $\tan(\beta)=\frac{F_{t,j}}{F_{n,j}}=\frac{K_tbh(\phi_j)}{K_nK_tbh(\phi_j)}=\frac{1}{K_n}$. The projections of the tangential and normal force components onto the fixed (x and y) coordinate frame are:

$$F_{x,j}=-F_{t,j}\cos(\phi_j)-F_{n,j}\sin(\phi_j) \text{ and } F_{y,j}=F_{t,j}\sin(\phi_j)-F_{n,j}\cos(\phi_j). \tag{4.3.14}$$

Substitution into the $F_{x,j}$ component gives Eq. 4.3.15.

$$\begin{aligned}F_{x,j}&=\begin{pmatrix}-(K_tb(\Delta x\cdot\sin(\phi_j)+\Delta y\cdot\cos(\phi_j))g(\phi_j))\cos(\phi_j)-\\ (K_nK_tb(\Delta x\cdot\sin(\phi_j)+\Delta y\cdot\cos(\phi_j))g(\phi_j))\sin(\phi_j)\end{pmatrix}\\ F_{x,j}&=-K_tbg(\phi_j)\begin{pmatrix}(\Delta x\cdot\sin(\phi_j)+\Delta y\cdot\cos(\phi_j))\cos(\phi_j)+\\ K_n(\Delta x\cdot\sin(\phi_j)+\Delta y\cdot\cos(\phi_j))\sin(\phi_j)\end{pmatrix}\\ F_{x,j}&=-K_tbg(\phi_j)\begin{pmatrix}\Delta x(\sin(\phi_j)\cos(\phi_j)+K_n\sin^2(\phi_j))+\\ \Delta y(\cos^2(\phi_j)+K_n\sin(\phi_j)\cos(\phi_j))\end{pmatrix}\end{aligned} \tag{4.3.15}$$

Similarly, the $F_{y,j}$ component is expressed as shown in Fig. 4.3.16.

$$
\begin{aligned}
F_{y,j} &= \begin{pmatrix} (K_t b(\Delta x \cdot \sin(\phi_j) + \Delta y \cdot \cos(\phi_j))g(\phi_j)) \sin(\phi_j) - \\ (K_n K_t b(\Delta x \cdot \sin(\phi_j) + \Delta y \cdot \cos(\phi_j))g(\phi_j)) \cos(\phi_j) \end{pmatrix} \\
F_{y,j} &= K_t b g(\phi_j) \begin{pmatrix} (\Delta x \cdot \sin(\phi_j) + \Delta y \cdot \cos(\phi_j)) \sin(\phi_j) - \\ K_n(\Delta x \cdot \sin(\phi_j) + \Delta y \cdot \cos(\phi_j)) \cos(\phi_j) \end{pmatrix} \\
F_{y,j} &= K_t b g(\phi_j) \begin{pmatrix} \Delta x(\sin^2(\phi_j) - K_n \cos(\phi_j) \sin(\phi_j)) + \\ \Delta y(\cos(\phi_j) \sin(\phi_j) - K_n \cos^2(\phi_j)) \end{pmatrix}
\end{aligned}
\tag{4.3.16}
$$

Substituting the trigonometric identities $\sin(\phi)\cos(\phi) = \frac{\sin(2\phi)}{2}$, $\sin^2(\phi) = \frac{1-\cos(2\phi)}{2}$, and $\cos^2(\phi) = \frac{1+\cos(2\phi)}{2}$ into Eqs. 4.3.15 and 4.3.16 yields:

$$
F_{x,j} = -\frac{1}{2} K_t b g(\phi_j) \begin{pmatrix} \Delta x(\sin(2\phi_j) + K_n(1 - \cos(2\phi_j))) + \\ \Delta y(1 + \cos(2\phi_j) + K_n \sin(2\phi_j)) \end{pmatrix} \text{ and} \tag{4.3.17}
$$

$$
F_{y,j} = \frac{1}{2} K_t b g(\phi_j) \begin{pmatrix} \Delta x((1 - \cos(2\phi_j)) - K_n \sin(2\phi_j)) + \\ \Delta y(\sin(2\phi_j) - K_n(1 + \cos(2\phi_j))) \end{pmatrix}. \tag{4.3.18}
$$

The force expressions are completed by including the summation over all teeth so that the contributions of (potentially) multiple teeth in the cut are considered.

$$
F_x = \sum_{j=1}^{N_t} F_{x,j} \text{ and } F_y = \sum_{j=1}^{N_t} F_{y,j} \tag{4.3.19}
$$

The x and y direction force expressions are now arranged in matrix form to obtain:

$$
\begin{pmatrix} F_x \\ F_y \end{pmatrix} = \frac{1}{2} b K_t \begin{bmatrix} a_{xx} & a_{xy} \\ a_{yx} & a_{yy} \end{bmatrix} \begin{pmatrix} \Delta x \\ \Delta y \end{pmatrix} = \frac{1}{2} b K_t [A](\Delta). \tag{4.3.20}
$$

where the individual A matrix entries, referred to in [5] as the “time varying directional dynamic force coefficients”, are:

$$a_{xx} = \sum_{j=1}^{N_t} -g(\phi_j)\left(\sin(2\phi_j) + K_n\left(1 - \cos(2\phi_j)\right)\right),$$

$$a_{xy} = \sum_{j=1}^{N_t} -g(\phi_j)\left(1 + \cos(2\phi_j) + K_n \sin(2\phi_j)\right),$$

$$a_{yx} = \sum_{j=1}^{N_t} g(\phi_j)\left(\left(1 - \cos(2\phi_j)\right) - K_n \sin(2\phi_j)\right), \text{and}$$

$$a_{yy} = \sum_{j=1}^{N_t} g(\phi_j)\left(\sin(2\phi_j) - K_n\left(1 + \cos(2\phi_j)\right)\right).$$

Here we note that, because these expressions are periodic with the tooth pitch, $\phi_p = \frac{2\pi}{N_t}$ (rad), they are also periodic in time over the tooth period, $\tau = \frac{60}{\Omega N_t}$ (s), where Ω is expressed in rpm. Therefore, although the A matrix is written as a function of ϕ in Eq. 4.3.20, it is equivalently a function of time, $t = \frac{\phi}{\Omega}\frac{60}{2\pi}$ (s), where Ω is given in rpm and ϕ in rad. In order to remove the time dependence of the A matrix, now written explicitly as $[A(t)]$, it is first expanded into a Fourier series:

$$[A(t)] = \sum_{r=-\infty}^{\infty} [A_r] e^{ir\omega_{tooth} t}, \tag{4.3.21}$$

where $\omega_{tooth} = 2\pi \cdot f_{tooth}$ (rad/s) and the Fourier coefficients are $[A_r] = \frac{1}{N_t \tau} \int_0^{N_t \tau} [A(t)] e^{-ir\omega_{tooth} t} dt$, and then only the $r = 0$ term is retained. Although $[A(t)]$ is best represented using multiple harmonics of ω_{tooth}, setting $r = 0$ leads to the desired time invariance because the exponential term becomes unity ($e^0 = 1$). The tradeoff is that the accuracy degrades as the radial immersion is reduced (the same is true for the average tooth angle approximation). This is particularly true when the radial immersion is only a few percent and the cutting force becomes more "impulse-like" [6–9]. Equation 4.3.22 shows the $r = 0$ coefficient, $[A_0]$, written explicitly as a function of ϕ (as in Eq. 4.3.20). By modifying the integration limits to be ϕ_s and ϕ_e (all angles in rad), the switching function is effectively removed since it is equal to one within these limits and zero otherwise.

$$[A_0] = \frac{1}{2\pi} \int_0^{2\pi} [A(\phi)] d\phi = \frac{1}{2\pi} \int_{\phi_s}^{\phi_e} [A(\phi)] d\phi = \frac{N_t}{2\pi} \begin{bmatrix} \alpha_{xx} & \alpha_{xy} \\ \alpha_{yx} & \alpha_{yy} \end{bmatrix} \tag{4.3.22}$$

The individual α terms, similar to the directional orientation factors defined in the average tooth angle approach, are provided in Eq. 4.3.23, where the integrals must be evaluated between ϕ_s and ϕ_e to obtain the final scalar values. Note that the N_t term is introduced in the final Eq. 4.3.22 expression due to the summations ($\sum_{j=1}^{N_t}\ldots$) in the a terms from Eq. 4.3.20.

$$\begin{aligned}
\alpha_{xx} &= \frac{1}{2}\left(\cos(2\phi) - 2K_n\phi + K_n\sin(2\phi)\right)\Big|_{\phi_s}^{\phi_e} \\
\alpha_{xy} &= \frac{1}{2}\left(-\sin(2\phi) - 2\phi + K_n\cos(2\phi)\right)\Big|_{\phi_s}^{\phi_e} \\
\alpha_{yx} &= \frac{1}{2}\left(-\sin(2\phi) + 2\phi + K_n\cos(2\phi)\right)\Big|_{\phi_s}^{\phi_e} \\
\alpha_{yy} &= \frac{1}{2}\left(-\cos(2\phi) - 2K_n\phi - K_n\sin(2\phi)\right)\Big|_{\phi_s}^{\phi_e}
\end{aligned} \tag{4.3.23}$$

The stability analysis begins by equating the frequency-domain vibrations in the x and y directions (the j subscripts indicate the current tooth) with the product of the frequency response function matrix and the frequency-domain representation of the cutting forces.

$$\begin{pmatrix} X_j \\ Y_j \end{pmatrix} = \begin{bmatrix} FRF_{xx} & FRF_{xy} \\ FRF_{yx} & FRF_{yy} \end{bmatrix} \begin{pmatrix} F_x \\ F_y \end{pmatrix} e^{i\omega_c t} = \begin{bmatrix} FRF_{xx} & 0 \\ 0 & FRF_{yy} \end{bmatrix} \begin{pmatrix} F_x \\ F_y \end{pmatrix} e^{i\omega_c t} \tag{4.3.24}$$

In Eq. 4.3.24, the cross FRFs (FRF_{xy}, representing measurement in the x direction with excitation in the y direction, and FRF_{yx}) are set equal to zero because the x and y directions are orthogonal and zero cross-talk between the two directions is assumed. Also, the ω_c notation indicates chatter frequencies (rad/s). The vibrations one tooth period earlier (denoted by the j–1 subscripts) are similarly written as:

$$\begin{pmatrix} X_{j-1} \\ Y_{j-1} \end{pmatrix} = \begin{pmatrix} X_j \\ Y_j \end{pmatrix} e^{-i\omega_c\tau} = \begin{bmatrix} FRF_{xx} & 0 \\ 0 & FRF_{yy} \end{bmatrix} \begin{pmatrix} F_x \\ F_y \end{pmatrix} e^{i\omega_c t} \cdot e^{-i\omega_c\tau}, \tag{4.3.25}$$

where $e^{-i\omega_c\tau}$ represents the delay of one tooth period. Taking the difference between Eqs. 4.3.24 and 4.3.25 gives:

$$\begin{pmatrix} X_j \\ Y_j \end{pmatrix} - \begin{pmatrix} X_{j-1} \\ Y_{j-1} \end{pmatrix} = \left(1 - e^{-i\omega_c\tau}\right) \begin{bmatrix} FRF_{xx} & 0 \\ 0 & FRF_{yy} \end{bmatrix} \begin{pmatrix} F_x \\ F_y \end{pmatrix} e^{i\omega_c t}. \tag{4.3.26}$$

The left hand side of Eq. 4.3.26 can be written as $\begin{pmatrix} X_j \\ Y_j \end{pmatrix} - \begin{pmatrix} X_{j-1} \\ Y_{j-1} \end{pmatrix} = \begin{pmatrix} \Delta X \\ \Delta Y \end{pmatrix}$, which enables substitution into the frequency-domain representation of Eq. 4.3.20, the "dynamic milling equation" according to [5].

$$\begin{pmatrix} F_x \\ F_y \end{pmatrix} e^{i\omega_c t} = \frac{1}{2} bK_t[A_0]\left(1 - e^{i\omega_c \tau}\right) \begin{bmatrix} FRF_{xx} & 0 \\ 0 & FRF_{yy} \end{bmatrix} \begin{pmatrix} F_x \\ F_y \end{pmatrix} e^{i\omega_c t} \tag{4.3.27}$$

Rearranging Eq. 4.3.27 gives

$\begin{pmatrix} F_x \\ F_y \end{pmatrix} e^{i\omega_c t} \left([I] - \frac{1}{2} bK_t(1 - e^{i\omega_c \tau})[A_0] \begin{bmatrix} FRF_{xx} & 0 \\ 0 & FRF_{yy} \end{bmatrix} \right) = 0$, which has a non-trivial solution only if:

$$\det\left([I] - \frac{1}{2} bK_t\left(1 - e^{i\omega_c \tau}\right)[A_0] \begin{bmatrix} FRF_{xx} & 0 \\ 0 & FRF_{yy} \end{bmatrix} \right) = 0, \tag{4.3.28}$$

where $[I] = \begin{bmatrix} 1 & 0 \\ 0 & 1 \end{bmatrix}$ is the 2×2 identity matrix. This is the characteristic equation of the closed loop dynamic milling system [5]. The product $[A_0][FRF]$ from Eq. 4.3.28 is analogous to the oriented FRF from the average tooth angle approach. Expanding gives Eq. 4.3.29.

$$\begin{gathered} [A_0][FRF] = \frac{N_t}{2\pi} \begin{bmatrix} \alpha_{xx} & \alpha_{xy} \\ \alpha_{yx} & \alpha_{yy} \end{bmatrix} \begin{bmatrix} FRF_{xx} & 0 \\ 0 & FRF_{yy} \end{bmatrix} = \\ \frac{N_t}{2\pi} \begin{bmatrix} \alpha_{xx} FRF_{xx} & \alpha_{xy} FRF_{yy} \\ \alpha_{yx} FRF_{xx} & \alpha_{yy} FRF_{yy} \end{bmatrix} = \frac{N_t}{2\pi} [FRF_{or}] \end{gathered} \tag{4.3.29}$$

A new variable, Λ, is now defined as:

$$\Lambda = \frac{N_t}{2\pi} \left(-\frac{1}{2} bK_t\left(1 - e^{-i\omega_c \tau}\right) \right) = -\frac{N_t}{4\pi} bK_t\left(1 - e^{-i\omega_c \tau}\right) \tag{4.3.30}$$

so that the characteristic equation can be rewritten as shown in Eq. 4.3.31, which includes the new oriented FRF, FRF_{or}, from Eq. 4.3.29.

$$\det([I] + \Lambda[FRF_{or}]) = 0 \tag{4.3.31}$$

Computing the determinant, $\det\begin{bmatrix} 1 + \Lambda\alpha_{xx} FRF_{xx} & \Lambda\alpha_{xy} FRF_{yy} \\ \Lambda\alpha_{yx} FRF_{xx} & 1 + \Lambda\alpha_{yy} FRF_{yy} \end{bmatrix} = 0$, gives an expression which is quadratic in Λ.

$$(1+\Lambda\alpha_{xx}FRF_{xx})\left(1+\Lambda\alpha_{yy}FRF_{yy}\right)-\Lambda^2\left(\alpha_{xy}FRF_{yy}\right)\left(\alpha_{yx}FRF_{xx}\right)=0$$
$$\Lambda^2\left(\alpha_{xx}\alpha_{yy}FRF_{xx}FRF_{yy}-\alpha_{xy}\alpha_{yx}FRF_{xx}FRF_{yy}\right)+\Lambda\left(\alpha_{xx}FRF_{xx}+\alpha_{yy}FRF_{yy}\right)+1=0$$

This frequency dependent equation is rewritten as $a_0\Lambda^2+a_1\Lambda+1=0$, where $a_0=FRF_{xx}FRF_{yy}\left(\alpha_{xx}\alpha_{yy}-\alpha_{xy}\alpha_{yx}\right)$ and $a_1=\alpha_{xx}FRF_{xx}+\alpha_{yy}FRF_{yy}$. The two roots are the system eigenvalues, Λ_1 and Λ_2. These complex eigenvalues can be determined using the quadratic equation:

$$\Lambda_{1,2}=\frac{-a_1\pm\sqrt{a_1^2-4a_0}}{2a_0}=-\frac{1}{2a_0}\left(a_1\mp\sqrt{a_1^2-4a_0}\right).$$

Note that these eigenvalues are a function of ω_c due to the dependence on the x and y direction FRFs. At each potential chatter frequency, the minimum b_{lim} value (from the two available eigenvalues) is selected to establish the limiting chip width. The relationship between b_{lim} and Ω is detailed next.

Equation 4.3.30 is now rewritten by recognizing the complex nature of the eigenvalues, $\Lambda=\Lambda_{\text{Re}}+i\Lambda_{\text{Im}}$, and substituting the Euler identity $e^{-i\omega_c\tau}=\cos(\omega_c\tau)-i\sin(\omega_c\tau)$:

$$\Lambda_{\text{Re}}+i\Lambda_{\text{Im}}=-\frac{N_t}{4\pi}bK_t(1-\cos(\omega_c\tau)+i\sin(\omega_c\tau)). \tag{4.3.32}$$

Equation 4.3.32 is solved for b to obtain the limiting chip width, b_{lim}:

$$b_{\text{lim}}=-(\Lambda_{\text{Re}}+i\Lambda_{\text{Im}})\frac{4\pi}{N_tK_t}\frac{1}{(1-\cos(\omega_c\tau)+i\sin(\omega_c\tau))}. \tag{4.3.33}$$

Rationalizing Eq. 4.3.33 gives Eq. 4.3.34.

$$\begin{aligned}
b_{\text{lim}}&=-(\Lambda_{\text{Re}}+i\Lambda_{\text{Im}})\frac{4\pi}{N_tK_t}\frac{(1-\cos(\omega_c\tau)-i\sin(\omega_c\tau))}{\left((1-\cos(\omega_c\tau))^2+(\sin(\omega_c\tau))^2\right)}\\
b_{\text{lim}}&=-\frac{4\pi}{N_tK_t}\frac{(\Lambda_{\text{Re}}+i\Lambda_{\text{Im}})(1-\cos(\omega_c\tau)-i\sin(\omega_c\tau))}{(2-2\cos(\omega_c\tau))}\\
b_{\text{lim}}&=-\frac{2\pi}{N_tK_t}\left(\begin{array}{c}\frac{(\Lambda_{\text{Re}}(1-\cos(\omega_c\tau))+\Lambda_{\text{Im}}\sin(\omega_c\tau))}{(1-\cos(\omega_c\tau))}+\\ i\frac{(\Lambda_{\text{Im}}(1-\cos(\omega_c\tau))-\Lambda_{\text{Re}}\sin(\omega_c\tau))}{(1-\cos(\omega_c\tau))}\end{array}\right)
\end{aligned} \tag{4.3.34}$$

Next, it is recognized that, because b_{lim} must be real valued, the imaginary part of the final expression in Eq. 4.3.34 must be equal to zero, giving $\Lambda_{\text{Im}}(1-\cos(\omega_c\tau))-\Lambda_{\text{Re}}\sin(\omega_c\tau)=0$. From this statement, the new variable κ is defined.

$$\kappa = \frac{\Lambda_{\mathrm{Im}}}{\Lambda_{\mathrm{Re}}} = \frac{\sin(\omega_c \tau)}{1 - \cos(\omega_c \tau)} \tag{4.3.35}$$

Equation 4.3.34 is now rewritten to obtain the final, frequency dependent expression for the stability limit.

$$\begin{aligned}
b_{\lim} &= -\frac{2\pi}{N_t K_t}\left(\frac{(\Lambda_{\mathrm{Re}}(1-\cos(\omega_c\tau)) + \Lambda_{\mathrm{Im}}\sin(\omega_c\tau))}{(1-\cos(\omega_c\tau))}\right)\\
b_{\lim} &= -\frac{2\pi}{N_t K_t}\left(\Lambda_{\mathrm{Re}} + \frac{\Lambda_{\mathrm{Im}}\sin(\omega_c\tau)}{(1-\cos(\omega_c\tau))}\right)\\
b_{\lim} &= -\frac{2\pi}{N_t K_t}\Lambda_{\mathrm{Re}}\left(1 + \frac{\Lambda_{\mathrm{Im}}}{\Lambda_{\mathrm{Re}}}\frac{\sin(\omega_c\tau)}{(1-\cos(\omega_c\tau))}\right) = -\frac{2\pi}{N_t K_t}\Lambda_{\mathrm{Re}}\left(1+\kappa^2\right)
\end{aligned} \tag{4.3.36}$$

The corresponding frequency dependent spindle speeds are determined by first writing the phase shift in the surface undulations between subsequent tooth passages (similar to the average tooth angle derivation), $\varepsilon = \pi - 2\psi$ (rad), where $\psi = \tan^{-1}(\kappa)$ (rad). The tooth passing periods are next expressed as $\tau = \frac{1}{\omega_c}(\varepsilon + j \cdot 2\pi)$ (s), where $j = 0, 1, 2\ldots$ refers to the integer number of waves between teeth. Incrementing j leads to the individual lobes; it serves in the same capacity as N in Eq. 4.3.2. Finally, the spindle speeds are obtained from:

$$\Omega = \frac{60}{N_t \tau}\,(\mathrm{rpm}). \tag{4.3.37}$$

Because our computing platform of choice is MATLAB®, we will rewrite the eigenvalue problem as stated in Eq. 4.3.31, $\det([I] + \Lambda[FRF_{or}]) = 0$, in the more traditional format required by the `eig` function. This formulation is $\det([FRF_{or}] - \lambda[I]) = 0$, where the new eigenvalue expression is $\lambda = \frac{4\pi}{N_t}\frac{1}{bK_t(1-e^{-i\omega_c\tau})}$. The corresponding revised stability limit is:

$$\tilde{b}_{\lim} = \frac{2\pi}{N_t K_t\left(\lambda_{\mathrm{Re}}^2 + \lambda_{\mathrm{Im}}^2\right)}\lambda_{\mathrm{Re}}\left(1+\tilde{\kappa}^2\right) \tag{4.3.38}$$

where $\tilde{\kappa} = \frac{\lambda_{\mathrm{Im}}}{\lambda_{\mathrm{Re}}}$. The derivation that leads to Eq. 4.3.38 is included in Appendix B. The two complex eigenvalues, λ_1 and λ_2, are determined using the MATLAB® function call `eig(FRF_or)` in p_4_3_6_1.m, where `FRF_or` is the oriented FRF defined in Eq. 4.3.29. The spindle speed equations are also modified to be $\tilde{\psi} = \tan^{-1}(\tilde{\kappa})$ (rad), $\tilde{\varepsilon} = \pi - 2\tilde{\psi}$ (rad), $\tilde{\tau} = \frac{1}{\omega_c}(\tilde{\varepsilon} + j \cdot 2\pi)(\mathrm{s})$ (s), and

$$\tilde{\Omega} = \frac{60}{N_t \tilde{\tau}}\,(\mathrm{rpm}). \tag{4.3.39}$$

The stability lobe diagram is obtained by plotting $\tilde{\Omega}$ versus the two $\tilde{b}_{\text{lim}}$ values for each chatter frequency (the minimum at each spindle speed is selected to define the stability boundary). Note that in this analysis the valid chatter frequencies are not limited to those corresponding to negative real values of the oriented FRF. Instead, the full frequency range of FRF_{or} is applied.

IN A NUTSHELL There are two related, but slightly different, methods for dealing with the varying orientation of the cutting force as the teeth pass through the cutting zone. Both approaches are simplifications of reality and have cutting conditions and machine dynamic characteristics where they predict experimental results more or less accurately.

Example 4.3.6: Comparison with Ex. 4.3.5 stability results In this example, the conditions are the same as for Ex. 4.3.5. Specifically, a 20% radial immersion down milling cut with a start angle of $\phi_s = 126.9$ deg and exit angle of $\phi_e = 180$ deg is analyzed. The x (feed) direction dynamics are $f_{nx} = 900$ Hz, $k_x = 9 \times 10^6$ N/m, and $\zeta_x = 0.02$. The y direction dynamics are $f_{ny} = 950$ Hz, $k_y = 1 \times 10^7$ N/m, and $\zeta_y = 0.01$. The workpiece material is a low carbon steel alloy and it is machined with a three tooth, 19 mm diameter square endmill. For a specific force value of $K_s = 2250$ N/mm^2 and a force angle of $\beta = 75$ deg, the corresponding cutting force coefficients are $K_n = \frac{1}{\tan(\beta)} = 0.268$ and $K_t = \frac{K_s}{\sqrt{1+K_n^2}} = 2173$ N/mm^2.

Based on the selected start and exit angles and K_n value, the α values from Eq. 4.3.23 required to calculate FRF_{or} are $\alpha_{xx} = 0.5198$, $\alpha_{xy} = -1.2356$, $\alpha_{yx} = 0.6180$, and $\alpha_{yy} = -1.0165$. The stability lobe diagram obtained from the Fourier series analysis is provided in Fig. 4.3.11. Two limits are seen; the dotted line is obtained from λ_1 and the solid line from λ_2. It is observed that the composite stability limit (defined collectively from the minimum of the λ_1 and λ_2 b_{lim} values at each spindle speed) is very similar to the average tooth angle limit shown in Fig. 4.3.9. For example, $b_{\text{lim,crit}} = 0.50$ mm from Fig. 4.3.11 compares favorably with the 0.41 mm value from Fig. 4.3.9 and the stability boundary peaks and troughs occur at the same spindle speeds. As noted previously, the MATLAB® program used to produce Fig. 4.3.11 is provided on the companion CD as p_4_3_6_1.m.

Example 4.3.7: Comparison with Ex. 4.3.4 stability results In contrast to the close agreement between the two approaches seen in Ex. 4.3.6, the methods diverge somewhat in the case of slotting. Although the best speeds agree, the allowable chip widths differ. As in Ex. 4.3.4, the symmetric x and y direction dynamics are $f_n = 500$ Hz, $k = 8 \times 10^6$ N/m, and $\zeta = 0.02$. An aluminum alloy is machined with a four tooth square endmill and the cutting force coefficients are $K_t = 695$ N/mm^2 and $K_n = 0.404$, corresponding to $K_s = 750$ N/mm^2 and

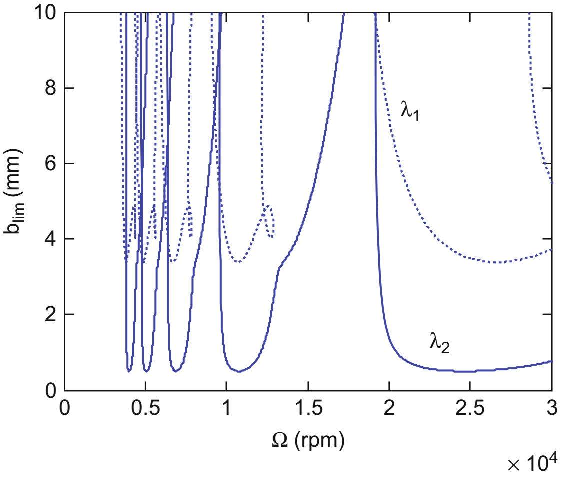

Fig. 4.3.11 Example 4.36 Stability lobe diagram ($j = 0$ to 4)

$\beta = 68$ deg. For $\phi_s = 0$ and $\phi_e = 180$ deg, the α values are $\alpha_{xx} = -1.2693$, $\alpha_{xy} = -3.1416$, $\alpha_{yx} = 3.1416$, and $\alpha_{yy} = -1.2693$.

The Fourier series approach stability limit is shown as the solid line in Fig. 4.3.12. Only the λ_1 boundary is seen at the selected scale (the λ_2 boundary occurs at higher chip widths in this case). For comparison convenience, the result from the average tooth angle approach (previously shown in Fig. 4.3.5) is also included as the dotted line. In this case, the $b_{\mathrm{lim,crit}}$ values are 0.22 mm (Fourier series) and 0.58 mm (average tooth angle). Additionally, the stable

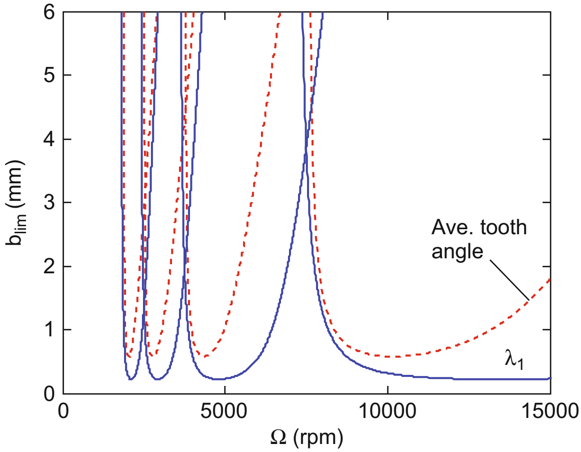

Fig. 4.3.12 Example 4.3.7 stability lobe diagram. The solid line shows the Fourier series stability boundary($j = 0$ to 3), while the dotted line gives the average tooth angle result ($N = 0$ to 3)

zone (beneath the stability boundary) has a smaller area for the Fourier series calculations. We will explore this disagreement further in Section 4.4. The MATLAB® program used to produce Fig. 4.3.12 is included as p_4_3_7_1.m on the companion CD.

4.4 Milling Time-Domain Simulation with Straight Teeth

In this section, a time-domain simulation for the milling problem is detailed. It is based on the 'Regenerative Force, Dynamic Deflection Model' described by Smith and Tlusty [10]. As with the turning analysis in Chapter 3, the analytical stability lobe diagrams detailed in Section 4.3 provide a "global" picture of the stability behavior, but do not provide information regarding the "local" cutting force or tool vibrations. The time-domain simulation, on the other hand, gives this "local" force and vibration information for the selected cutting conditions. The simulation again applies numerical integration to solve the time delayed differential equations of motion and includes the nonlinearity that occurs if the tooth leaves the cut. Assumptions include straight cutter teeth, the circular tool path, and a square endmill geometry. Similar to turning, the simulation proceeds as follows: 1) the instantaneous chip thickness is determined using the vibration of the current and previous teeth at the selected tooth angle; 2) the cutting force is calculated; 3) the force is used to find the new displacements; and 4) the tooth angle is incremented and the process is repeated. The simulation model geometry is the same as was presented in Fig. 4.1.8. We use modal parameters to describe the dynamics of the non-rigid tool in the x and y directions, where multiple degrees of freedom in each direction can be accommodated as described in Section 3.5.

IN A NUTSHELL Nothing is a better representation of reality than reality (actual cutting). However, milling simulation removes many of the simplifying assumptions required by the analytical derivations. As in turning, time-domain simulation provides detailed information about a specific case, but loses the global information provided by the analytical solutions. The production of a stability lobe diagram requires many executions of the simulation.

4.4.1 Chip Thickness Calculation

The instantaneous chip thickness depends on the nominal, tooth angle dependent chip thickness (Eq. 4.1.2), the current normal direction vibration, and the vibration of the previous tooth at the same angle. As described in Section 4.2, the chip thickness can be expressed as $h(t) = f_t \sin(\phi) + n(t - \tau) - n(t)$, where τ

is the tooth period, $\tau = \frac{60}{\Omega N_t}$ (s) and Ω is given in rpm. The vibrations in the direction of the surface normal for the current tooth depend on the x and y vibrations as well as the tooth angle, according to $n = x\sin(\phi) - y\cos(\phi)$. Figure 4.2.5 presented an "unwrapped" view of the milled surface that demonstrates the regeneration mechanism in the chip thickness equation. Note that the positive x direction again opposes the feed direction. For this simulation, we will neglect the possibility that the current surface may depend on more than the prior and current tooth vibrations (as shown for turning in Fig. 3.5.1). Also, because we have assumed straight teeth, we will ignore vibrations in the z direction.

As discussed in the stability lobe development, the milling equations may be equivalently considered to be a function of time or angle. For the simulation, our strategy is to divide the angle of the cut into a discrete number of steps. At each small time step, dt, we increment the cutter angle by the corresponding small angle, $d\phi$. This approach enables convenient computation of the chip thickness for each simulation step because: 1) we have predefined the possible teeth orientations; and 2) we can store the surface created by the previous tooth at each angle. The cutter rotation by the $d\phi$ increment is depicted in Fig. 4.4.1, where the size of the increment depends on the selection of the number of steps per revolution (`steps _rev` in p_4_4_1_1.m on the companion CD), specifically, $d\phi = \frac{360}{steps\_rev}$ (deg). The corresponding time step is $dt = \frac{60}{steps\_rev \cdot \Omega}$ (s), where Ω is the spindle speed in rpm. (Note that the teeth number labeling convention differs from that shown in Sections 4.1 and 4.2. Previously, the teeth were numbered according to their order of entry into the cut for convenience of description, while they are now labeled according to increasing angle in a clockwise manner for "bookkeeping" purposes within the simulation.) A vector of angles is defined to represent the potential orientations of the teeth as the cutter is rotated through one revolution of the circular tool path, $\phi = [0, d\phi, 2d\phi, 3d\phi, \ldots, (steps\_rev - 1)d\phi]$. The locations of the teeth within the cut are then defined by referencing entries in this vector (`phi` in p_4_4_1_1.m). For

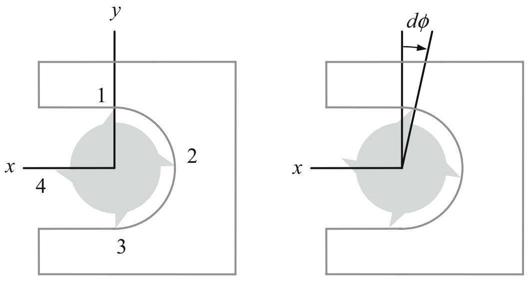

Simulation step: *cnt* Simulation step: *cnt* + 1

Fig. 4.4.1 Cutter rotation by $d\phi$ from one simulation step to the next (a slotting cut is depicted) equal teeth spacing, this means that the teeth are located every $\frac{steps\_rev}{N_t}$. A vector of tooth orientations, that indicates particular entries in the ϕ vector, not actual angles, is then defined as: $teeth = [1, \frac{steps\_rev}{N_t} + 1, 2\frac{steps\_rev}{N_t} + 1, \ldots, (N_t - 1)\frac{steps\_rev}{N_t} + 1]$. Incrementing the teeth angles by $d\phi$ is then a simple matter of adding one to each entry in the *teeth* vector. Finally, individual tooth angles can be identified by the MATLAB® statement: `phi (teeth(cnt))` indicates the tooth in question. Therefore, a requirement for using the $\frac{steps\_rev}{N_t}$ ratio to indicate locations within the ϕ vector is that it is an integer greater than zero (necessary for MATLAB® indices). This is explored in Ex. 4.4.1.

Example 4.4.1: Simulation tooth angle definition We'll consider the case where 650 steps per revolution has been selected for a cutter with four teeth. The spindle speed is 10000 rpm. Our first requirement is that $\frac{steps\_rev}{N_t}$ is an integer so that the `phi` vector can be referenced using the `teeth` entries. In this case, $\frac{steps\_rev}{N_t} = \frac{650}{4} = 162.5$ steps/tooth. To correct the non-integer situation, the MATLAB® function `round` can be implemented to determine the nearest integer ratio:

```
temp = round(steps_rev/Nt);
steps_rev = temp*Nt;
```

as shown in p_4_4_1_1.m. The result is that the new ratio, saved to the `temp` variable, is 163 and the updated number of steps per revolution is 652. The angular increment is $d\phi = \frac{360}{652} = 0.5521$ deg and the time increment for numerical integration is $dt = \frac{60}{652.10000} = 9.2025 \times 10^{-6}$ s. The vector of possible tooth angles (in MATLAB® syntax) is `phi = [ 0 0.5521 1.1043 1.6564 ... 359.4479]` deg and the *teeth* vector can be initially described by `teeth = [ 1 164 327 490]`. For this cutter orientation, tooth 1 is positioned at `phi (teeth(1)) = phi(1) = 0`. Similarly, the angles for teeth 2 through 4 are `phi(teeth(2)) = phi(164) = 90` deg, `phi(teeth(3)) = phi(327) = 180` deg, and `phi(teeth(4)) = phi(490) = 270` deg, respectively. In the next time increment, 9.2025×10^{-6} s later, the *teeth* vector values are each incremented by one to be `teeth = [ 2 165 328 491]`. The teeth angles are `phi(teeth(1)) = phi(2) = 0.5521` deg, `phi(teeth (2)) = phi(165) = 90.5521` deg, `phi(teeth(3)) = phi(328) = 180.5521` deg, and `phi(teeth (4)) = phi(491) = 270.5521` deg.

The next step in determining the (discrete) chip thickness at each simulation step is to address the $n(t - \tau)$ and $n(t)$ terms in the continuous $h(t) = f_t \sin(\phi) + n(t - \tau) - n(t)$ chip thickness equation. The $n(t)$ term is simply the current normal direction vibration level determined using:

```
n = (x*sin(phi(teeth(cnt3))*pi/180) - y*cos(phi
(teeth(cnt3))*pi/180));
```

in p_4_4_1_1.m, where `x` and `y` are the current x and y direction vibrations, the `sin` and `cos` functions require arguments in rad, and `cnt3` is a simulation index that counts through the individual teeth to sum the force contributions.

To accommodate the $n(t-\tau)$ term, the normal direction vibration for the previous tooth at the current angular orientation is required. To organize these values, a new variable *surf*[3] is defined. Values in this vector are indexed in the same way as `phi` (according to entries in the *teeth* vector), i.e., `surf (teeth(cnt3))`. The *surf* entries are updated after the current chip thickness calculation so that each time the value is queried at a particular orientation, the entry for that tooth angle is referencing the result from the last time a tooth was positioned at the current angle. There are two scenarios for updating the `surf` value. First, if the current tooth is cutting (it is between ϕ_s and ϕ_e and the tangential cutting force is greater than or equal to zero), then the value is set to the current vibration using:

```
surf(teeth(cnt3)) = n;
```

in p_4_4_1_1.m. Recall that this value will not be referenced until the next tooth is at the current angle. Second, if the current tooth is bounded by the start and exit angles, but the tangential force is less than zero, then the tooth has vibrated out of the cut and the updating command is:

```
surf(teeth(cnt3)) = surf(teeth(cnt3)) + ft*sin(phi
(teeth(cnt3))*pi/180);
```

so that the previous value is appended by the nominal feed per tooth that was not removed. If the current angle is not bounded by the cut, then no updating is necessary. Finally, the instantaneous chip thickness equation is:

```
h = ft*sin(phi(teeth(cnt3))*pi/180) + surf(teeth
(cnt3)) - n;
```

in p_4_4_1_1.m.

4.4.2 Force Calculation

Once the chip thickness is computed, the tangential component of the force in the current time step is determined using Eq. 4.1.8, where the chip width, *b*, is equal to the axial depth of cut for straight teeth. As with turning, the calculated chip thickness is negative if the current tool vibration in the normal direction is larger than the surface location (equal to the sum of the nominal chip thickness, $f_t \sin\phi$, and the vibration of the previous tooth at the same angle). The tangential cutting force is set to zero in this situation that no cutting is occurring. The normal force is then computed and these results are projected into the *x* and *y* directions as shown in Eqs. 4.1.11 and 4.1.12.

---

[3] This variable is named to indicate the machined surface, not surfing along Florida's Atlantic coast.

4.4.3 Displacement Calculation

Considering a single degree of freedom in the x and y directions, the equations of motion are:

$$m_x\ddot{x} + c_x\dot{x} + k_x x = F_{x_1} \text{ and } m_y\ddot{y} + c_y\dot{y} + k_y y = F_{y_1}. \tag{4.4.1}$$

Rewriting Eq. 4.4.1 yields expressions for the x and y direction accelerations in the current time step:

$$\ddot{x} = \frac{F_x - c_x\dot{x} + k_x x}{m_x} \text{ and } \ddot{y} = \frac{F_y - c_y\dot{y} + k_y y}{m_y}. \tag{4.4.2}$$

where the velocities, $\dot{x}$ and $\dot{y}$, and positions, x and y, from the previous time step are used (initial values are zero to begin the simulation). The new velocities and positions are then determined by numerical (Euler) integration:

$$\dot{x} = \dot{x} + \ddot{x} \cdot dt \qquad \dot{y} = \dot{y} + \ddot{y} \cdot dt \tag{4.4.3}$$

$$x = x + \dot{x} \cdot dt \qquad y = y + \dot{y} \cdot dt, \tag{4.4.4}$$

where the velocities on the right hand side of the equal signs in Eq. 4.4.3 are retained from the previous time step. The new velocities are then applied to determine the new displacements in Eq. 4.4.4. Again, the displacements on the right hand side of Eq. 4.4.4 are those from the previous time step. As mentioned previously, multiple degrees of freedom in each direction can be accommodated by summing the individual modal contributions as described in Section 3.5. Again, considering the dynamic characteristics of the machine in a modal sense facilitates the computation.

4.4.4 Simulation Summary and Implementation

The milling simulation provided in p_4_4_1_1.m completes three basic activities at each time step. First, the cutter is rotated by $d\phi$ by adding one to each entry in the *teeth* vector. Second, within a `for` loop (indexed by `cnt3`) that sums over all the cutter teeth, it is first verified that the tooth in question is bounded by the start and exit cut angles. If so, the chip thickness is determined and the cutting force is calculated (including the nonlinearity if a tooth leaves the cut due to excessive vibration). If not, the force is set to zero. Third, the displacement is determined by numerical integration. To exercise the simulation, comparisons between the stability limits described in Ex. 4.3.7 and the simulated forces and displacements are made in Ex. 4.4.2.

Example 4.4.2: Comparison with Ex. 4.3.7 using time-domain simulation To review, the x and y direction dynamics are symmetric with $f_n = 500$ Hz,

$k = 8 \times 10^6$ N/m, and $\zeta = 0.02$. An aluminum alloy is machined with a four tooth square endmill and the cutting force coefficients are $k_t = 695$ N/mm^2 and $k_n = 281$ N/mm^2, corresponding to $K_s = 750$ N/mm^2 and $\beta = 68$ deg. For the slotting cut, $\phi_s = 0$ and $\phi_e = 180$ deg. Additionally, there are 652 steps per revolution, the feed per tooth is 0.15 mm/tooth, and 20 revolutions are simulated, where the number of revolutions (*rev*) is related to the total number of simulation steps (*steps*) by $rev = \frac{steps \cdot dt \cdot \Omega}{60}$. Four different cases are considered: 1) $\Omega = 7500$ rpm and $b = 3$ mm; 2) $\Omega = 7500$ rpm and $b = 5$ mm; 3) $\Omega = 5000$ rpm and $b = 0.1$ mm; and 4) $\Omega = 5000$ rpm and $b = 0.5$ mm. These operating points are identified in Fig. 4.4.2, which includes the average tooth angle and Fourier series stability limits.

According to the two analytical approaches, cases 1 and 3 should provide stable operating conditions. The time-domain simulation corroborates these predictions. Figures 4.4.3 and 4.4.4 show the x and y direction forces and displacements, respectively, for case 1. It is seen that, once the initial transients attenuate after approximately 0.07s, the expected constant force for a four tooth cutter in a slotting cut is obtained. Similar results are observed for case 3 in Figs. 4.4.5 and 4.4.6.

For cases 2 and 4, however, the Fourier series approach predicts that the cuts will be unstable, while the average tooth angle approximation shows these should be stable conditions. Figures 4.4.7 and 4.4.8 display the x and y direction results for case 2. Chatter is observed with the forces and displacement increasing over time. Additionally, Fig. 4.4.9 shows the resultant force and nonlinearity when the force drops to zero as the tooth vibrates out of the cut (in the vicinity of 0.1 s for example). Similar results are seen for case 4 in Figs. 4.4.10

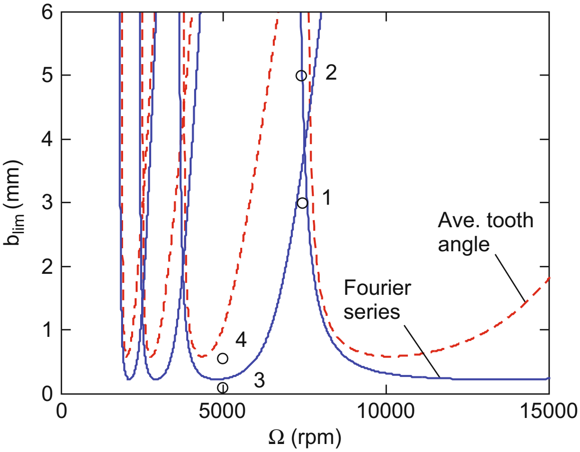

Fig. 4.4.2 Operating points for comparison between analytical stability boundaries from Ex. 4.3.7 and time-domain simulation. 1) $\Omega = 7500$ rpm and $b = 3$ mm; 2) $\Omega = 7500$ rpm and $b = 5$ mm; 3) $\Omega = 5000$ rpm and $b = 0.1$ mm; and 4) $\Omega = 5000$ rpm and $b = 0.5$ mm

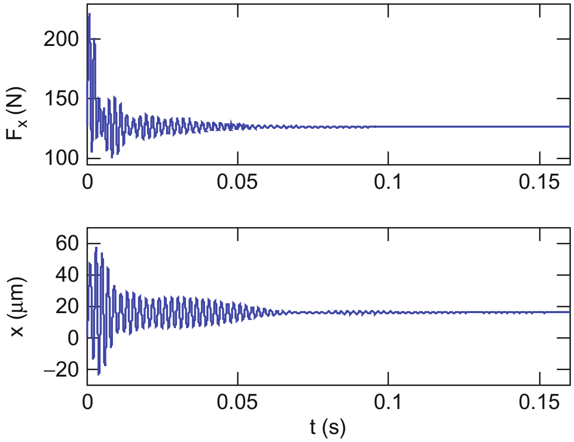

Fig. 4.4.3 Example 4.4.2 stable case 1 ($\Omega = 7500$ rpm and $b = 3$ mm) simulation results for x direction force (top) and displacement (bottom)

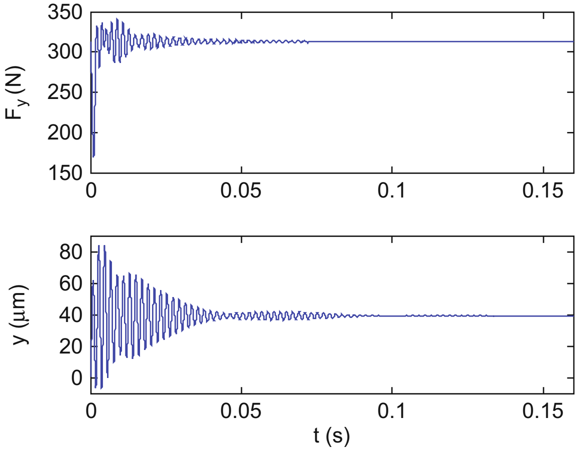

Fig. 4.4.4 Example 4.4.2 stable case 1 ($\Omega = 7500$ rpm and $b = 3$ mm) simulation results for y direction force (top) and displacement (bottom)

through 4.4.12. Here the vibration and force levels grow quickly until the nonlinearity is reached and then the levels persist. The disagreement between the average tooth angle stability boundary and time-domain simulation for cases 2 and 4 is due to the orthogonality between the average surface normal and y direction in slotting. This causes the directional orientation factor for the y direction, μ_y, to be zero (see Ex. 4.3.4) and the contribution of the dynamics in the y direction to be neglected. The simulation used to produce Figs. 4.4.3 through 4.4.12 is included as p_4_4_1_1.m on the companion CD.

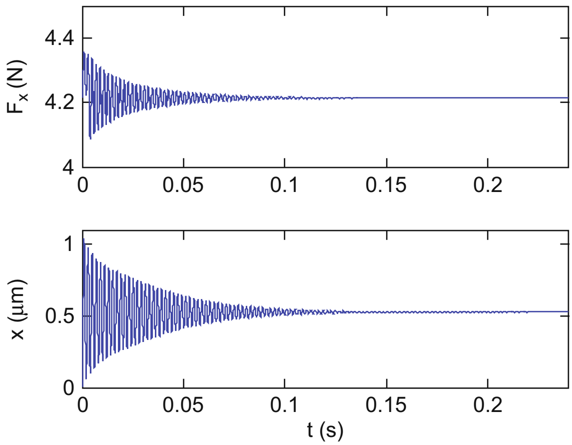

Fig. 4.4.5 Example 4.4.2 stable case 3 ($\Omega = 5000$ rpm and $b = 0.1$ mm) simulation results for x direction force (top) and displacement (bottom)

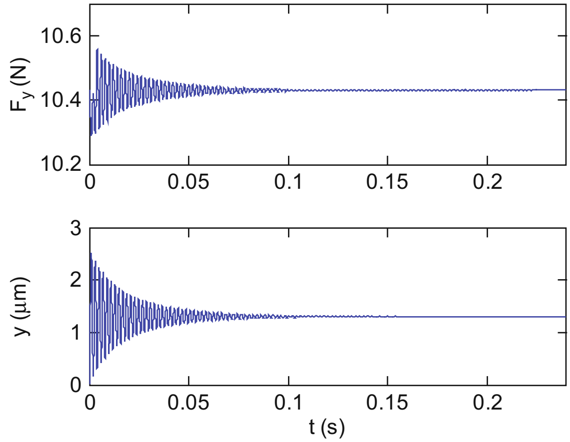

Fig. 4.4.6 Example 4.4.2 stable case 3 ($\Omega = 5000$ rpm and $b = 0.1$ mm) simulation results for y direction force (top) and displacement (bottom)

Example 4.4.3: Comparison with Ex. 4.3.6 using time-domain simulation The milling conditions are 20% radial immersion down milling cut with a start angle of $\phi_s = 126.9$ deg and exit angle of $\phi_e = 180$ deg. The x direction dynamics are $f_{nx} = 900$ Hz, $k_x = 9 \times 10^6$ N/m, and $\zeta_x = 0.02$. The y direction dynamics are $f_{ny} = 950$ Hz, $k_y = 1 \times 10^7$ N/m, and $\zeta_y = 0.01$. The workpiece material is a low carbon steel alloy and it is machined with a three tooth, 19 mm diameter square endmill and feed per tooth of 0.2 mm/tooth. For a specific force value of $K_s = 2250$ N/mm^2 and a force angle of $\beta = 75$ deg, the corresponding cutting

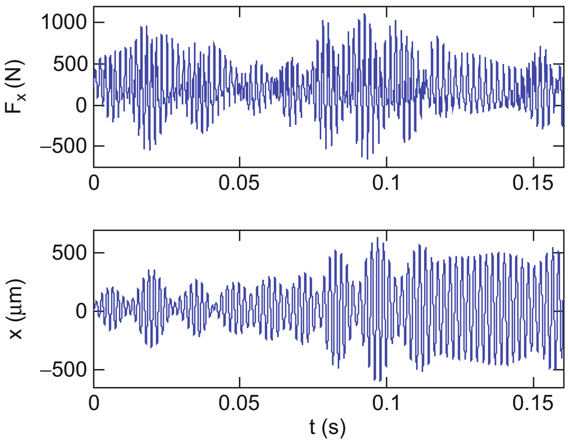

Fig. 4.4.7 Example 4.4.2 unstable case 2 ($\Omega = 7500$ rpm and $b = 5$ mm) simulation results for x direction force (top) and displacement (bottom)

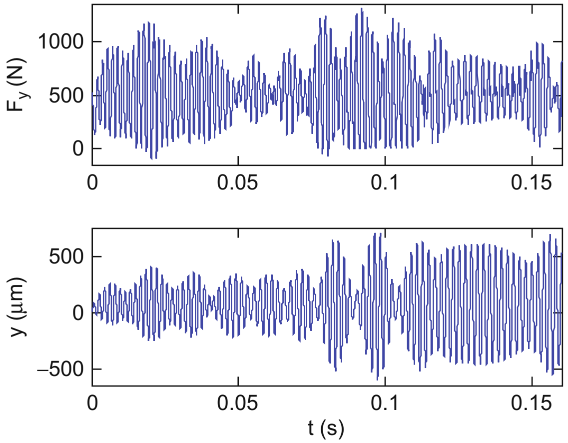

Fig. 4.4.8 Example 4.4.2 unstable case 2 ($\Omega = 7500$ rpm and $b = 5$ mm) simulation results for y direction force (top) and displacement (bottom)

force coefficients are $k_t = 2173$ N/mm^2 and $k_n = 582$ N/mm^2. The number of steps per revolution is 801 and 40 revolutions are simulated.

Based on the analytical stability lobe results in Figs. 4.3.9 and 4.3.11, let's select two (Ω, b) combinations for numerical simulation. Case 1 with $\Omega = 17000$ rpm and $b = 4$ mm should be stable according to the stability lobes. Case 2 with $\Omega = 13000$ rpm and $b = 4$ mm should be unstable. Figure 4.4.13 displays the y direction force and vibration for case 1. It takes approximately half of the first 40 revolutions for the transients to attenuate, but the final result is stable cutting. The force and vibrations results between 0.13 s and 0.14 s are

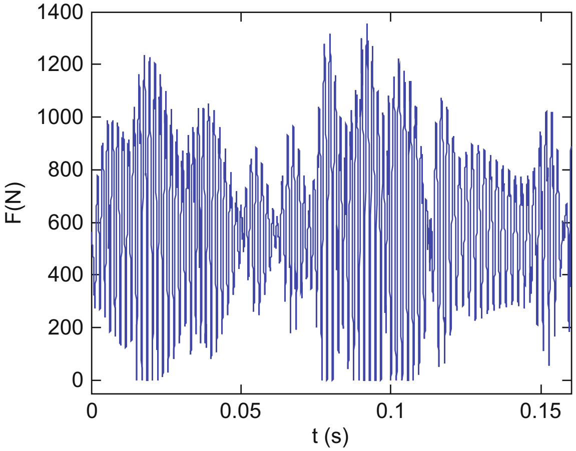

Fig. 4.4.9 Example 4.4.2 unstable case 2 ($\Omega = 7500$ rpm and $b = 5$ mm) simulation results for resultant force

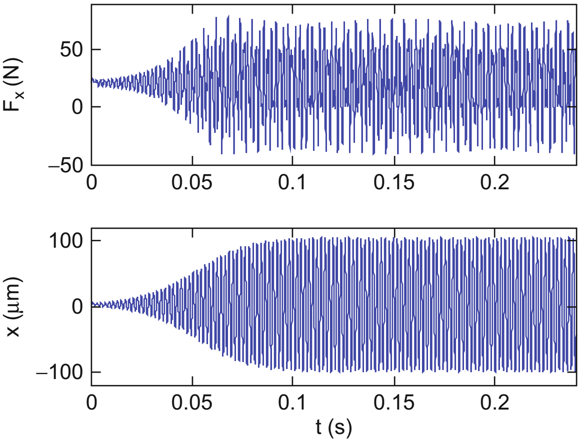

Fig. 4.4.10 Example 4.4.2 unstable case 4 ($\Omega = 5000$ rpm and $b = 0.5$ mm) simulation results for x direction force (top) and displacement (bottom)

displayed in Fig. 4.4.14. We see the expected force profile for the down milling cut. Note that only one tooth is engaged at any time so the force drops to zero during the delay between one tooth leaving the cut and the next tooth entering the cut (we refer to this as interrupted cutting). Also, the force is largest at the cut entry when the chip thickness is at is maximum value for down milling and drops to zero as the chip thickness decreases to zero, according to $f_t \sin(\phi)$, at the cut exit. The resulting tool vibrations are sinusoidal in nature.

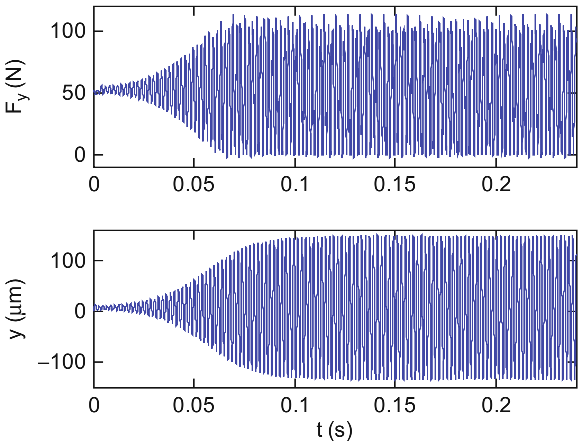

Fig. 4.4.11 Example 4.4.2 unstable case 4 ($\Omega = 5000$ rpm and $b = 0.5$ mm) simulation results for y direction force (top) and displacement (bottom)

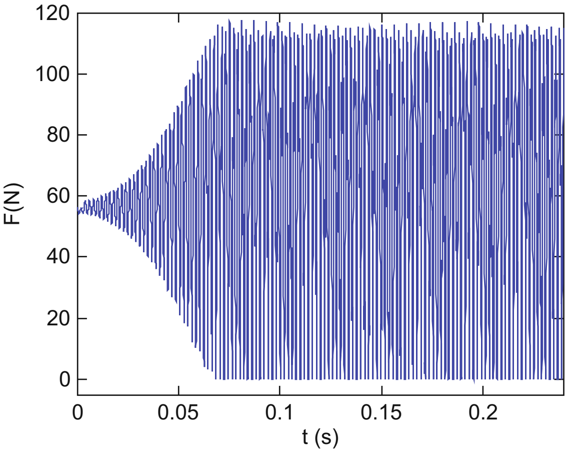

Fig. 4.4.12 Example 4.4.2 unstable case 4 ($\Omega = 5000$ rpm and $b = 0.5$ mm) simulation results for resultant force

The y direction force and vibration for case 2 are provided in Fig. 4.4.15. The behavior differs substantially from Figs. 4.4.14 and 4.4.15. For the previous stable cut (case 1), the vibration exhibited only a forced vibration response to the cutting force. For the unstable case 2, the vibration now occurs at both the chatter frequency (near the tool's natural frequency) and the forcing frequencies (the tooth passing frequency and its harmonics as demonstrated in Fig. 4.1.15). We will examine the frequency content of stable and unstable milling signals further in Chapter 6. Figure 4.4.16 shows the portion of the force and vibration

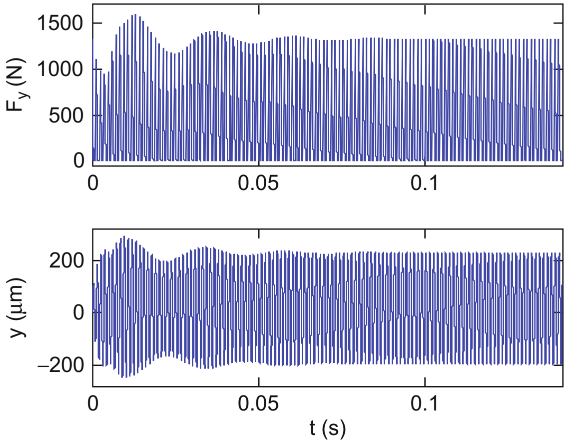

Fig. 4.4.13 Example 4.4.3 stable case 1 ($\Omega = 17000$ rpm and $b = 4$ mm) simulation results for y direction force (top) and displacement (bottom)

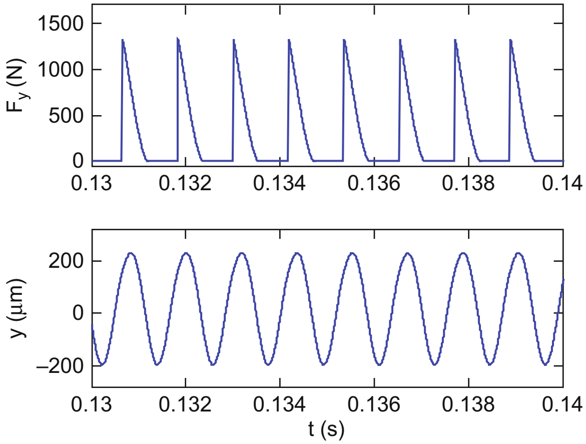

Fig. 4.4.14 Portion of results from Fig. 4.4.13 between 0.13 s and 0.14 s

between 0.13 and 0.16 s. The behavior is clearly different than the stable case shown in Fig. 4.4.14. The simulation used to produce the figures for this example is included as p_4_4_3_1.m on the companion CD.

4.5 Milling Time-Domain Simulation with Helical Teeth

While the simulation described in Section 4.4 is capable of predicting forces and displacement in milling, the assumption of straight cutter teeth is rarely applicable in practice. As discussed in Section 4.1, the cutting edges are typically

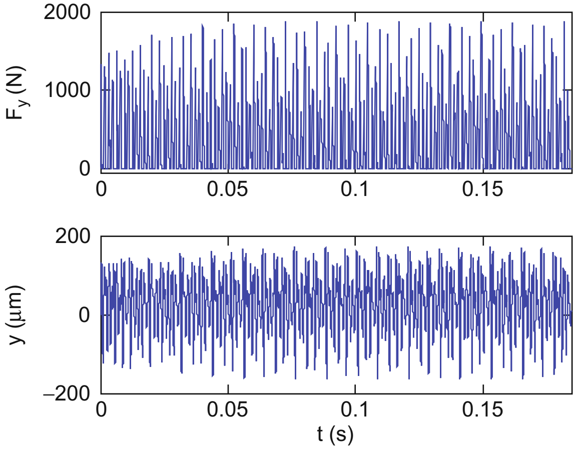

Fig. 4.4.15 Example 4.4.3 unstable case 2 ($\Omega = 13000$ rpm and $b = 4$ mm) simulation results for y direction force (top) and displacement (bottom)

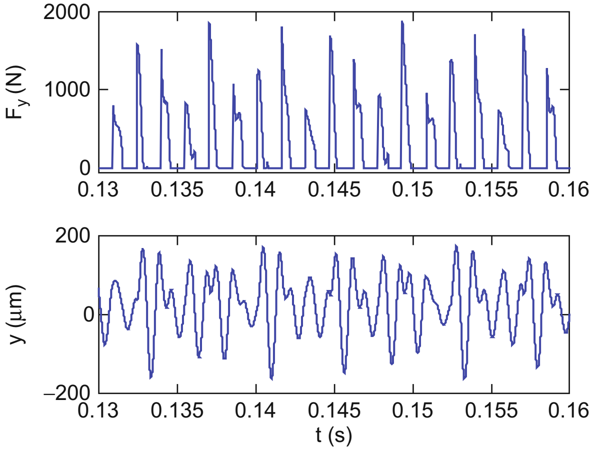

Fig. 4.4.16 Portion of results from Fig. 4.4.15 between 0.13 s and 0.16 s

inclined at the helix angle, γ, so that the chip to be removed is spread over an increased length and the cutting edge pressure is reduced. The result of the helical cutting edge geometry is that the full length of the cutting edge does not enter (or exit) the cut at the same instant. Instead, there is an increasing delay of the cut entry (and exit) when moving from the free end of the cutter toward the spindle. The situation is depicted in Fig. 4.5.1 for the helical square endmill geometry considered in this section.

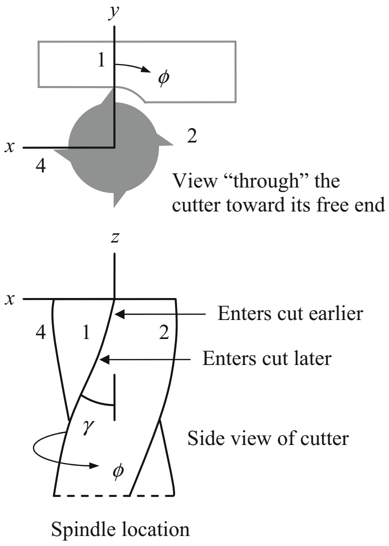

Fig. 4.5.1 The helical endmill geometry causes the cutting edge to enter and exit the cut at later instants in time when moving from its free end toward the spindle

We can visualize the angular delay, χ, of the helical cutting edge, which increases with distance from the cutter free end, by "unrolling" the periphery of the cylindrical endmill as described in [11]. The helical teeth now appear as straight lines and angles, ϕ (in rad), become distances, $r\phi$, where r is the endmill radius. Note that the velocity of every point on the tooth edge is the cutting speed, v (Eq. 4.1.17), with a direction perpendicular to the z axis. The unrolled view of the endmill pictured in Fig. 4.5.1 is presented in Fig. 4.5.2. The delay distance, $r\chi$, is zero at $z = 0$ (endmill free end) because we have referenced the cutter rotation angle, ϕ, to this axial location. However, at $z = -b$ the delay distance is now:

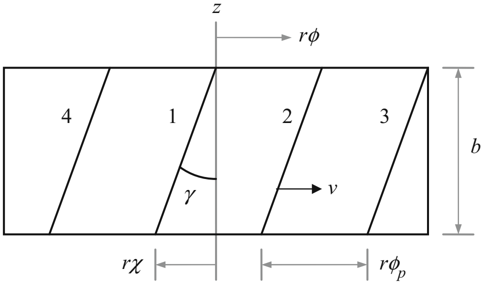

Fig. 4.5.2 Unrolled view of helical endmill geometry. The helical teeth appear as straight lines and angles are seen as distances

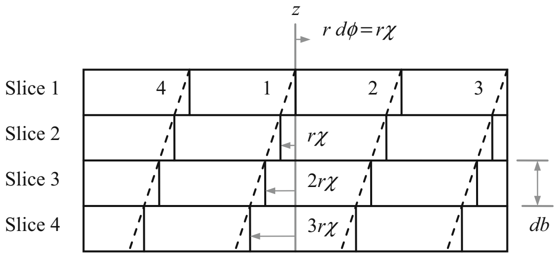

Fig. 4.5.3 Discretized version of unrolled helical endmill geometry. The axial depth is sectioned into multiple slices with thickness *db*. Each slice is treated as a straight tooth cutter with the delay distance $r\chi = r\, d\phi$ relative to the adjacent slice nearer the free end of the endmill

$$r\chi = b\tan(\gamma). \tag{4.5.1}$$

In order to discretize this relationship and retain the $d\phi$ angular increments in our time-domain simulation, we section the tool into a number of slices (or disks) perpendicular to the z axis. Each slice is treated as an individual straight tooth endmill, where the thickness of each slice is a small fraction, *db*, of the axial depth of cut, *b*. This approximation is shown in Fig. 4.5.3. Note that each slice incorporates the distance delay $r\chi = db\tan(\gamma)$ relative to the prior slice (nearer the cutter free end), which becomes the angular delay between slices of:

$$\chi = \frac{db\tan(\gamma)}{r} = \frac{2db\tan(\gamma)}{d}(\text{rad}) \tag{4.5.2}$$

for the rotating endmill. In Eq. 4.5.2, *d* is the endmill diameter. In order to ensure that the angles for each axial slice match the `phi` vector entries in the time-domain simulation, we require that the delay angle between slices is $\chi = d\phi$. This places a constraint on the *db* value. By substituting $d\phi$ for χ in Eq. 4.5.2 and rearranging, we see that we must select it such that:

$$\text{db} = \frac{d \cdot d\phi}{2\tan(\gamma)}. \tag{4.5.3.}$$

The integer number of axial slices for the simulation is then determined using the MATLAB® expression: `steps_axial = round(b/db)`. Naturally, the accuracy is improved if $db << b$, which requires that $d\phi$ is small (i.e., the `steps_ rev` value is high).

The primary modifications to the time-domain simulation described in Section 4.4 are that: 1) an additional `for` loop is added to count through the individual axial slices (`cnt4` in p_4_5_1_1.m included on the companion CD); and 2) the `surf` vector is now replaced by an array, where each row in the array includes the `surf` information for a single axial slice. This array is also named `surf` in p_4_5_1_1.m. It is organized similar to Fig. 4.5.3, where the first row, `surf(1, 1:steps_rev)`, contains the data for the axial slice nearest the free end of the cutter ($z = 0$) and there are `steps_axial` total rows. Within the `cnt4` loop, the angle of the current axial slice, `phia`, is determined by decrementing the angle for the tooth in question, referenced to the free end of the cutter and indexed by `cnt3` in the next outer `for` loop, by: `phi_counter = teeth(cnt3) – (cnt4-1)`. Because we selected `db` using Eq. 4.5.3 to ensure that the angular delay corresponds to `dphi` between slices, the current axial slice angle is then: `phia = phi(phi_counter)`.

A secondary modification in p_4_5_1_1.m, relative to p_4_4_1_1.m and p_4_4_3_1.m, is that a vector notation for the modal parameters, velocities, and displacements is added. This new format enables the convenient inclusion of multiple modes in the models of the system dynamics for the x and y directions. For each mode in the x direction, for example, a separate numerical integration is completed to update the modal velocity, `dp(cnt5)`, and displacement, `p(cnt5)`, where `cnt5` is the mode number index. Because the response in local (physical) coordinates is the sum of the modal contributions, the individual modal displacements are simply added to obtain the x direction displacement. The y direction approach is the same, except the modal velocities and displacement are contained in the `dq` and `q` vectors, respectively. Strictly speaking, due to the helical geometry, we should also consider the axial (z direction) forces and potential deflections. However, for most endmilling applications, the z direction dynamic stiffness is much higher than the x or y direction stiffness values, so it is common to consider the z direction to be rigid.

Finally, because these simulations tend to take longer than the straight tooth cases, a progress bar has been added (for the impatient among us). The MATLAB® function `waitbar` was used to accomplish this task[4].

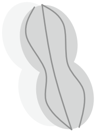

IN A NUTSHELL Because the teeth are helical, the portion of each tooth that is engaged in the cut varies as the tool rotates. The changing deflection of the tool is imprinted on the machined surface parallel to the tools' axis of rotation. It is difficult to include this complexity in the analytical formulations, but relatively straightforward to include in the time-domain simulation. For this and many other reasons, time-domain simulation is a better representation of the cutting process than either of the analytical formulations described earlier. As with all of engineering, however, there is an inherent trade-off to be made. In this case, it is that increased accuracy is computationally more intensive.

Example 4.5.1: Comparison of forces between straight and helical teeth In this example, we compare the cutting forces produced by straight and helical teeth with all other conditions being equal. We model a 30% radial immersion up milling cut with a zero start angle and exit angle of 66.4 deg. There are two

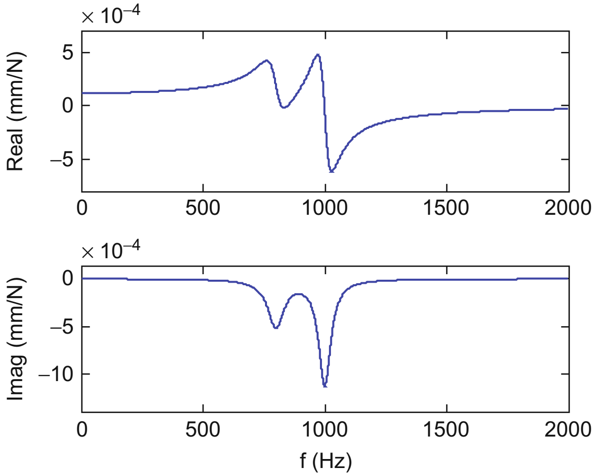

Fig. 4.5.4 Two mode FRF for Ex. 4.5.1 (x and y direction responses are equal)

identical modes in both the x and y directions. These are expressed in modal coordinates as: $f_{n1} = 800$ Hz, $k_{q1} = 2 \times 10^7$ N/m, and $\zeta_{q1} = 0.05$; and $f_{n2} = 1000$ Hz, $k_{q2} = 1.5 \times 10^7$ N/m, and $\zeta_{q2} = 0.03$. The FRF in local coordinates for these modal parameters is displayed in Fig. 4.5.4. The workpiece material is an aluminum alloy and it is machined with a four tooth, 19 mm diameter square endmill using a feed per tooth of 0.15 mm/tooth. For a specific force value of $K_s = 600$ N/mm^2 and force angle of $\beta = 60$ deg, the corresponding cutting force coefficients are $k_t = 520$ N/mm^2 and $k_n = 300$ N/mm^2 or, equivalently, $K_t = 520$ N/mm^2 and $K_n = 0.577$.

We wish to consider stable cutting conditions for the time-domain force simulations. To aid in the selection of stable (Ω, b) combinations, we first generate the stability lobe diagrams using the average tooth angle and Fourier series approaches. The directional orientation factors for the average tooth angle approach are $\mu_x = \cos(\beta - 56.8)\cos(56.8)$ and $\mu_y = \cos(146.8 - \beta)\cos(146.8)$ as described in Ex. 4.3.3, where the average tooth angle in the cut is now 33.2 deg. The stability lobe diagrams for the two analytical methods are shown in Figs. 4.5.5 and 4.5.6. We observe that the stability limits are similar and a preferred speed is near 15000 rpm. This agrees with the best spindle speed selection rule given in Eq. 4.3.7 even though this is a two degree of freedom system. The MATLAB® program p_4_5_1_2.m (available on the companion CD) was used to generate these two figures.

$$\Omega_{best} = \frac{f_n \cdot 60}{(N+1) \cdot N_t} = \frac{1000 \cdot 60}{(0+1) \cdot 4} = 15000 \text{ rpm}$$

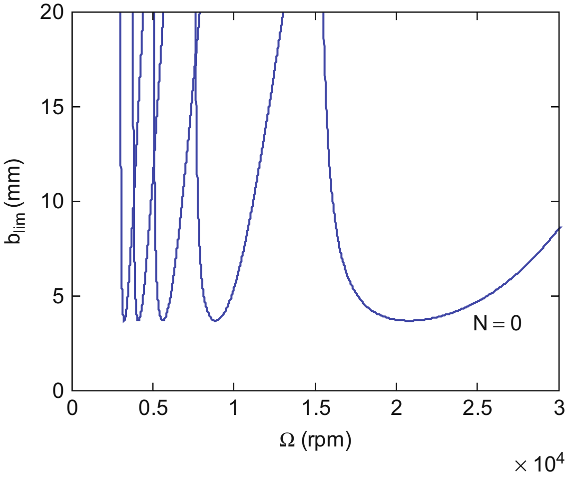

Fig. 4.5.5 Stability lobe diagram for Ex. 4.5.1 using average tooth angle approach (N = 0 to 4)

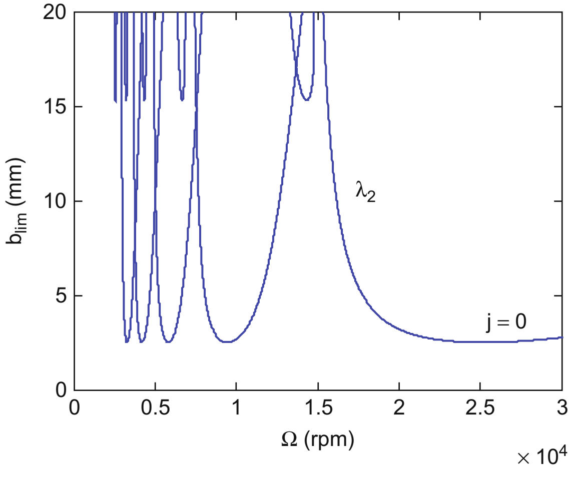

Fig. 4.5.6 Stability lobe diagram for Ex. 4.5.1 using Fourier series approach (j = 0 to 4)

For the time-domain simulations, let's choose the number of steps per revolution to be 800 and the number of revolutions to be 30. The spindle speed is 15000 rpm and two axial depths of cut are considered. Figures 4.5.7 and 4.5.8 show the resultant cutting forces (in the x-y plane) for a small time portion of the simulation result with b = 5 mm and helix angles of zero and 45 deg, respectively. A comparison of the two figures shows clear differences. First, the maximum cutter force is lower for the helical teeth endmill. Second, the force grows to its maximum value and then abruptly drops to zero at the cut

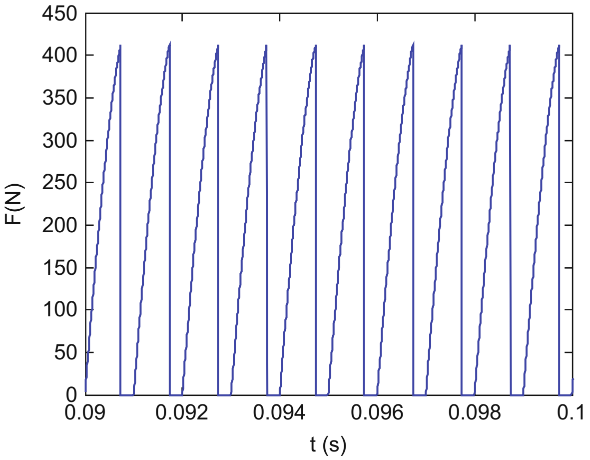

Fig. 4.5.7 Resultant cutting force versus time for zero helix angle endmill with $\Omega = 15000$ rpm and $b = 5$ mm

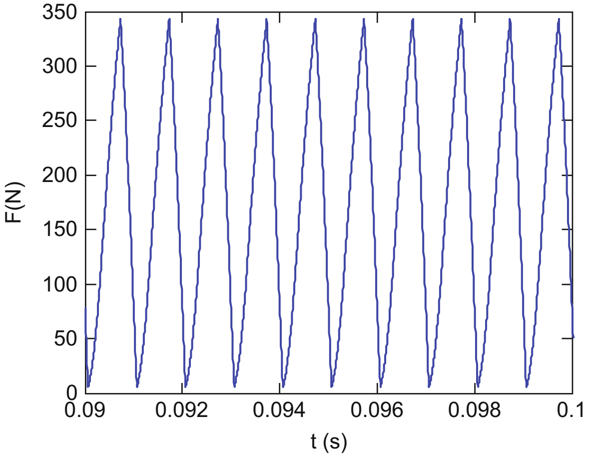

Fig. 4.5.8 Resultant cutting force versus time for 45 deg helix angle endmill with $\Omega = 15000$ rpm and $b = 5$mm

exit angle for the straight tooth endmill. For the helical teeth cutter, on the other hand, the force grows and then decreases in a more saw tooth pattern and does not quite reach zero. We can understand this behavior using Eq. 4.5.2 and Fig. 4.5.2. The lag angle between the free end of the cutter and the helical edge at $b = 5$ mm is $\chi = \frac{2b\tan(\gamma)}{d} = \frac{2\cdot5\tan(45)}{19} = 30.2$ deg. This means that the cutter rotates 30.2 deg between the time that the free end of the helical tooth enters the cut (assume that $\phi = 0$ here) and the time that the helical edge at $b = 5$ mm is engaged. At $\phi = 66.4$ deg, the free end cutting edge begins to exit the cut, but the helical portion nearer the spindle remains engaged. The force therefore does not drop immediately to zero. In fact, it does not drop to zero at all because, by the time the $b = 5$ mm helical portion exits the cut (30.2 deg later), the next tooth has entered the cut (i.e., $30.2 + 66.4 = 96.6$ deg is greater than the tooth pitch of 90 deg).

As noted in [11, Example 9.12], this "wrapping" behavior of the helical cutting edge can be exploited to achieve a constant cutting force at particular axial depths of cut. These b values are obtained when the lag angle is equal to the pitch angle. In this case, the same cutting edge length is engaged regardless of the cutter angle or radial depth of cut. The situation is depicted in Fig. 4.5.9, where the left gray box covers the cutting edge length for tooth 1. At a later instant in time, the right gray box represents the same lag distance for the helical endmill. Although tooth 1 is no longer engaged, we see that the same cutting edge length is covered but it is now made up of portions of teeth 2 and 3. This constant cutting edge length leads to the same force value for the two instants. The b value at which this behavior is observed is determined by rewriting Eq. 4.5.3 to be: $b = \frac{d \cdot \phi_p}{2\tan(\gamma)}$. For this example (45 deg helix with four teeth), the axial depth for constant cutting force is:

$$b = \frac{d \cdot \phi_p}{2\tan(\gamma)} = \frac{19 \cdot 90\frac{\pi}{180}}{2\tan(45)} = 14.9\,\text{mm}$$

Multiples of this axial depth will yield the same constant force behavior provided the cutting conditions remain stable (and sufficient flute length is available), although this is unlikely for typical tool-workpiece combinations.

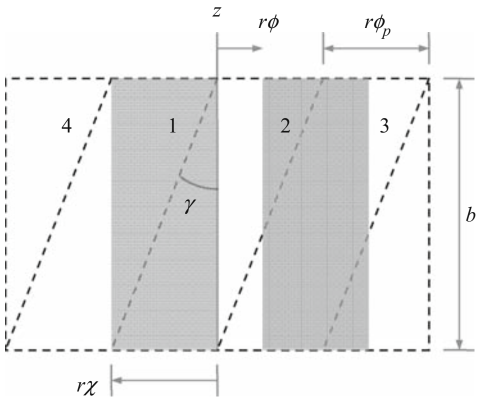

Fig. 4.5.9 when the lag angle is equal to the pitch angle, the same length of cutting edge is engaged regardless of the cutter angle (as shown by the two gray boxes). The force is constant for this axial depth

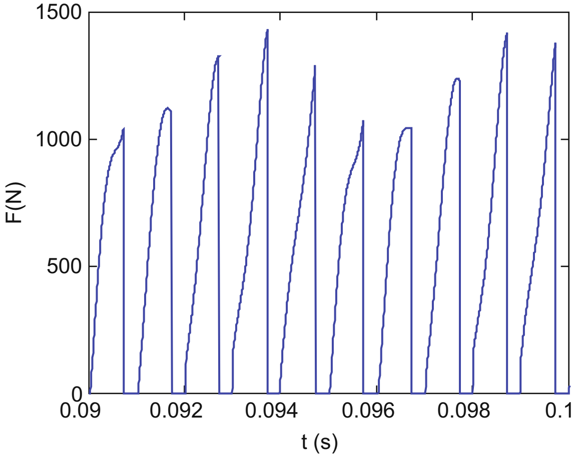

Fig. 4.5.10 Resultant cutting force versus time for 45 deg helix angle endmill with Ω = 15000 rpm and b = 14.9 mm

Figures 4.5.10 and 4.5.11 show the resultant forces for $\Omega = 15000$ rpm and $b = 14.9$ mm with helix angles of zero and 45 deg, respectively. It is seen that the cut is bordering on instability in Fig. 4.5.10; the force is disturbed from its nominal values by regeneration. In Fig. 4.5.11, however, the force is nearly constant with a small oscillation that is retained from the initial transients. Note that the same force scale is used on both plots. Clearly, the maximum force is much lower for the helical cutter. Figures 4.5.8 through 4.5.11 were produced using program p_4_5_1_1.m.

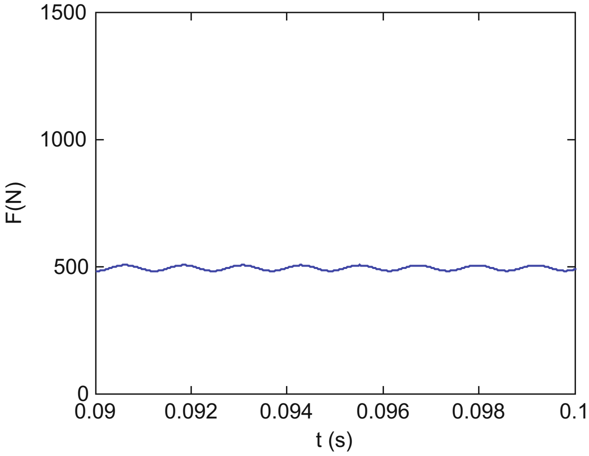

Fig. 4.5.11 Resultant cutting force versus time for 45 deg helix angle endmill with Ω = 15000 rpm and b = 14.9 mm

4.6 Ball Milling Time-Domain Simulation with Helical Teeth

In this section we extend the helical teeth milling simulation for square endmills from Section 4.5 to incorporate the spherical geometry of ball endmills. The circular tool path assumption is again applied. Additionally, the tool is sectioned into slices along its axis, as before, and the tool axis is perpendicular to the feed direction (in practice, the ball endmill axis is often inclined with respect to the feed direction to avoid cutting with the zero velocity point at the ball apex, but we will not treat this case). The ball endmilling simulation geometry and variables are displayed in Fig. 4.6.1, where we now compute the z direction force component although we maintain our assumption of rigid z direction dynamics. As shown, the width of the axial slices along the tool axis is dz. This value is again selected to ensure that the instantaneous cutter angle is coincident with one of the predefined `phi` angles as in Section 4.5. See Eq. 4.6.1, where γ is the global helix angle (the local helix on the spherical end varies with the z location as described in [12]).

$$dz = \frac{d \cdot d\phi}{2\tan(\gamma)} \tag{4.6.1}$$

The new variable, κ', is identified in Fig. 4.6.1 (the prime is used to differentiate it from the variable κ used in the Fourier series stability analysis). This represents the angle between the tool axis and the ball surface normal for the current axial slice and is calculated using Eq. 4.6.2, where j is the axial slice in question (`cnt4` in p_4_6_1_1.m) and r is the radius. It is used to first project the chip thickness from the x-y plane onto the tool surface normal direction and, second, project the tangential, normal, and axial force components onto the x-y-z coordinate directions (together with the tooth angle) [12].

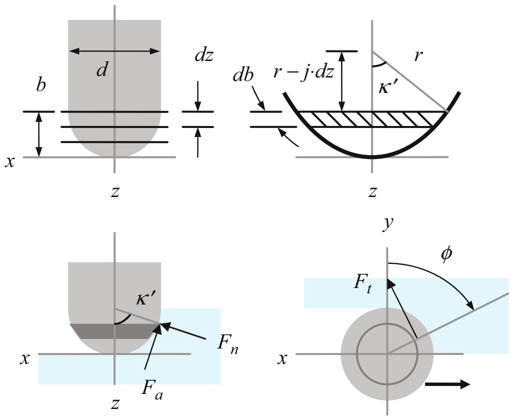

Fig. 4.6.1 Ball endmilling simulation geometry. The normal force component, F_n, is oriented along the ball surface normal

$$\kappa' = \cos^{-1}\left(1 - \frac{j \cdot dz}{r}\right) = \cos^{-1}\left(1 - \frac{2j \cdot dz}{d}\right) \tag{4.6.2}$$

As with the helical square endmill simulation, the instantaneous chip thickness in the *x*-*y* plane is determined from the: 1) nominal chip thickness, which depends on the feed per tooth and angle of the current tooth for the selected slice, `phia`; 2) vibrations in the *x* and *y* directions from the previous tooth, collected in the `surf` array (defined in the same way as described in Section 4.5); and 3) the *x* and *y* vibrations of the current tooth projected in the radial direction (i.e., the direction from the current tooth toward the tool axis in the *x*-*y* plane – this was the normal direction, `n`, for the helical square endmill simulation p_4_5_1_1.m). However, the *x*-*y* plane thickness must then be projected onto the ball surface normal direction using κ' (`kappa_p`). The relevant lines from the MATLAB® program p_4_6_1_1.m are provided here.

```
n = x*sin(phia*pi/180) - y*cos(phia*pi/180);
h = (ft*sin(phia*pi/180) + surf(cnt4, phi_counter)
    - n)*sin(kappa_p);
```

In addition to calculating the chip thickness, the chip width for each slice, *db*, must also be determined. While this was simply the width of each axial slice for the square endmill geometry, it is now the arc length of the current slice when cutting with the ball surface. The situation is depicted in Fig. 4.6.2, where the arc length is the product of the radius and the angle θ. See Eq. 4.6.3. The angle θ is, in turn, the difference between κ' and θ', $\theta = \kappa' - \theta'$. The angle θ' is defined in Eq. 4.6.4.

$$db = r\theta \tag{4.6.3}$$

$$\theta' = \cos^{-1}\left(\frac{r - dz(j-1)}{r}\right) = \cos^{-1}\left(1 - \frac{dz(j-1)}{r}\right) = \cos^{-1}\left(1 - \frac{2dz(j-1)}{d}\right) \tag{4.6.4}$$

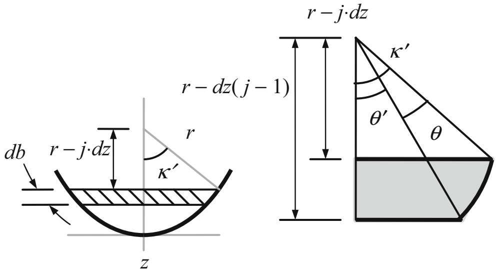

Fig. 4.6.2 Geometry for chip width, *db*, calculation when cutting on ball surface

Once the chip thickness and width are determined, the cutting force components in the tangential, normal, and axial directions are determined for each axial slice. See Eqs. 4.6.5 through 4.6.7 (referring to the F_a component as axial is actually something of a misnomer since it is directed along the tool axis only when κ' is 90 deg). Notice that a new cutting force coefficient, k_a, is defined in Eq. 4.6.7. It fills the same role as k_t and k_n, to relate the force to chip area, and is expressed in units of N/mm^2, or equivalent.

$$F_t = k_t hdb \tag{4.6.5}$$

$$F_n = k_n hdb \tag{4.6.6}$$

$$F_a = k_a hdb \tag{4.6.7}$$

As shown in Fig. 4.6.1, the projection of these components on the x-y-z fixed coordinate frame depends on both the instantaneous cutter angle, ϕ, and the ball surface normal direction, κ', for the selected tooth and slice. The force relationships are provided in matrix form in Eq. 4.6.8, where ϕ_a is the tooth angle `phia` from the MATLAB® program p_4_6_1_1.m.

$$\begin{Bmatrix} F_x \\ F_y \\ F_z \end{Bmatrix} = \begin{bmatrix} \cos(\phi_a) & \sin(\phi_a)\sin(\kappa') & -\sin(\phi_a)\cos(\kappa') \\ \sin(\phi_a) & -\cos(\phi_a)\sin(\kappa') & \cos(\phi_a)\cos(\kappa') \\ 0 & -\cos(\kappa') & -\sin(\kappa') \end{bmatrix} \begin{Bmatrix} F_t \\ F_n \\ F_a \end{Bmatrix} \tag{4.6.8}$$

The only remaining issue that must be addressed in the simulation is treating the case where the commanded axial depth is greater than the ball radius. In this situation κ' is set to 90 deg and Eq. 4.6.8 collapses to Eq. 4.6.9. The x and y force projections are now identical to the helical square endmill simulation and the z component is equal to the axial force (with the appropriate sign convention applied).

$$\begin{Bmatrix} F_x \\ F_y \\ F_z \end{Bmatrix} = \begin{bmatrix} \cos(\phi_a) & \sin(\phi_a) & 0 \\ \sin(\phi_a) & -\cos(\phi_a) & 0 \\ 0 & 0 & -1 \end{bmatrix} \begin{Bmatrix} F_t \\ F_n \\ F_a \end{Bmatrix} \tag{4.6.9}$$

Example 4.6.1: Comparison of forces between square and ball endmills Here we compare the cutting forces produced by helical square and ball endmills. As in Ex. 4.5.1, we consider a 30% radial immersion up milling cut with a zero start angle and exit angle of 66.4 deg with an axial depth of 5 mm (which is less than the tools' radii of 9.5 mm). The dynamic responses in the two directions are the same as was previously presented. The workpiece material is an aluminum alloy and it is assumed that the cutting force coefficients are the same for both four tooth endmills. For a specific force value of $K_s = 600$ N/mm^2 and force angle of $\beta = 60$ deg, the corresponding cutting force coefficients are $k_t = 520$ N/mm^2

and $k_n = 300\ \mathrm{N/mm^2}$ and the axial coefficient, k_a, is taken to be equal to k_n. The feed per tooth is 0.15 mm/tooth.

For the simulations, let's use 1200 steps per revolution and complete 10 full revolutions. Results for the cutting forces in the x, y, and z directions under these conditions are displayed in Figs. 4.6.3 through 4.6.5, respectively (the time span includes data that follows the attenuation of the initial transients). Differences are observed in all three directions. This is due to the variation in the ball surface normal angle and the corresponding

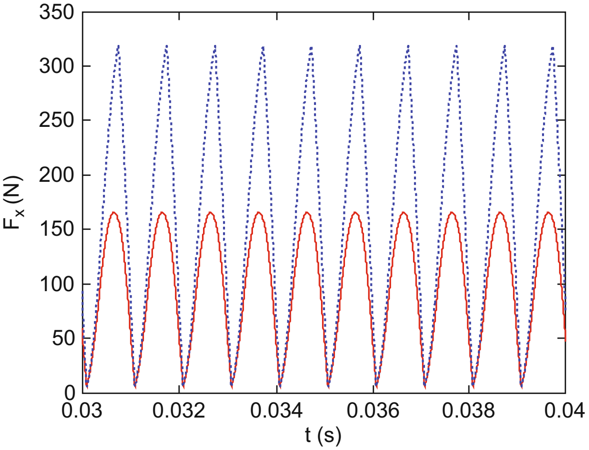

Fig. 4.6.3 Comparison of x direction cutting force for ball (solid line) and square (dotted line) helical endmills

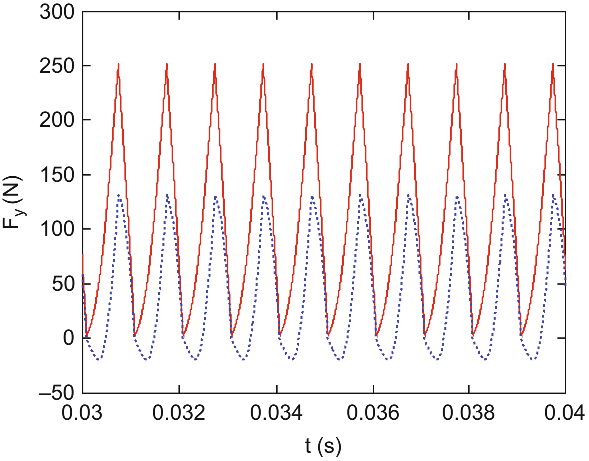

Fig. 4.6.4 Comparison of y direction cutting force for ball (solid line) and square (dotted line) helical endmills

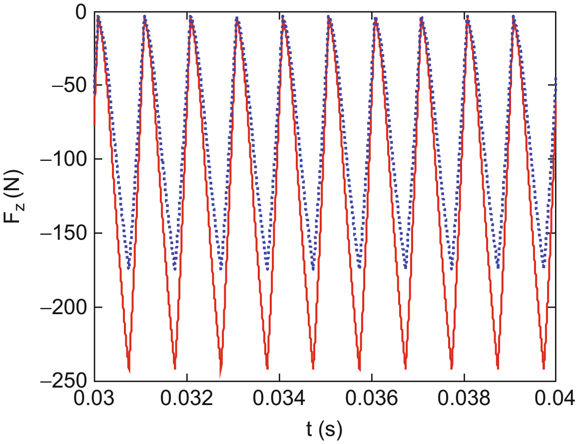

Fig. 4.6.5 Comparison of z direction cutting force for ball (solid line) and square (dotted line) helical endmills

projections of the normal and axial components according to Eq. 4.6.8. Naturally, the resultant force, $F = F_x^2 + F_y^2 + F_z^2$, is the same for both endmills. The MATLAB® programs p_4_6_1_1_.m (helical ball endmilling) and p_4_6_1_2_.m (helical square endmilling) may be used to obtain Figs. 4.6.3 through 4.6.5.

4.7 Experimental Cutting Force Coefficients

To conclude this chapter, let's discuss experimental determination of the cutting force coefficients for the milling force model (a square endmill geometry is again presumed). As shown in Fig. 4.1.8, these tests are carried out by prescribing a known feed per tooth and axial depth and measuring the x (feed), y, and z (axial) direction cutting force components in the dynamometer's fixed coordinate frame. Prior to detailing the numerical and experimental techniques used to obtain the coefficient values, however, let's revisit the force model and corresponding coefficients.

4.7.1 Updated Force Model

Equations 4.1.6 through 4.1.10 and 4.3.12 are all based on the assumption that the resultant cutting force, F in Fig. 4.1.7, is directly proportional to the chip thickness (and axial depth) and independent of other operating parameters. Although this is a reasonable assumption for the development of stability lobe diagrams used to guide the selection of preferred spindle speeds, comparison with measured cutting forces can show discrepancies with this approximation. First, because the cutting edge radius is nonzero, as the chip thickness is reduced to values near the edge radius there is increased rubbing[5] between the cutting edge and work surface which leads to a larger cutting force than the $F = K_s bh$ model would predict. With respect to chip formation in orthogonal cutting (Section 3.1), the rake angle, or inclination of the cutting edge relative to the surface normal, depends on both the chip thickness and edge radius in this case and can become negative if the ratio is unity or smaller, although the tool may have been designed with a positive rake angle at the macroscopic level. This rubbing phenomenon can be incorporated in the force model by adding a constant, or DC, force component that scales with the axial depth only, such that the force is nonzero even as the chip thickness approaches zero. This is referred to as the "edge effect" in [13] and threshold value in [14]. Additionally, the force may not linearly increase with chip thickness, but could follow a power law such as $F = K_s bh^c$, where c is a positive constant less than one [14]. Second, due to the variation in strain rate, temperature, and subsequent chip formation behavior, decreases in cutting force can be observed for higher cutting speeds [15]. This imposes a spindle speed dependence on the cutting force coefficients. Both of these issues (rubbing effect and cutting speed dependence) highlight the notion that these coefficients should not be considered material properties of the workpiece, but rather as approximate descriptions of the process behavior which depend on the tool-workpiece combination and, to a lesser extent, the operating conditions. Additional investigations of cutting force modeling may be reviewed in [16–26].

In order to improve the accuracy of the cutting force model without introducing significant complexity, let's augment Eqs. 4.1.7 and 4.1.8 to incorporate edge effects. Equations 4.7.1 and 4.7.2 now each include two coefficients: one is associated with "cutting" (or shearing) and includes the chip thickness dependence; and the other is the "rubbing" (or plowing) term, which is independent of chip thickness (denoted by the "e" subscript extension). We note that the DC rubbing terms, $k_{ne}b$ and $k_{te}b$, would be neglected in our analytical linear stability analyses anyway, so this does not invalidate our previous stability lobe diagram derivations. We have also added the axial force term in Eq. 4.7.3, which was neglected in our straight tooth analysis.

$$F_n = k_n bh + k_{ne} b \tag{4.7.1}$$

$$F_t = k_t bh + k_{te} b \tag{4.7.2}$$

$$F_a = k_a bh + k_{ae} b \tag{4.7.3}$$

---

[5] Plowing (alternately ploughing), or plastic deformation without material removal, can also occur for significant interference between the tool relief surface and workpiece.

We determine the six coefficients via linear regression using the average cutting forces measured by the dynamometer over a range of feed per tooth values. Projection of the normal and tangential components into the x, y, and z directions for the square endmill geometry, as shown in Fig. 4.1.8, gives Eqs. 4.7.4 through 4.7.6.

$$F_x = k_t b f_t \sin(\phi)\cos(\phi) + k_{te} b \cos(\phi) + k_n b f_t \sin^2(\phi) + k_{ne} b \sin(\phi) \tag{4.7.4}$$

$$F_y = k_t b f_t \sin^2(\phi) + k_{te} b \sin(\phi) - k_n b f_t \sin(\phi)\cos(\phi) - k_{ne} b \cos(\phi) \tag{4.7.5}$$

$$F_z = -k_a b f_t \sin(\phi) - k_{ae} b \tag{4.7.6}$$

If we apply the double angle identities: $\sin(\phi)\cos(\phi) = \frac{\sin(2\phi)}{2}$ and $\sin^2(\phi) = \frac{1-\cos(2\phi)}{2}$, we obtain Eqs. 4.7.7 and 4.7.8. The z direction force equation is unchanged.

$$F_x = k_t b f_t \frac{\sin(2\phi)}{2} + k_{te} b \cos(\phi) + k_n b f_t \frac{(1-\cos(2\phi))}{2} + k_{ne} b \sin(\phi) \tag{4.7.7}$$

$$F_y = k_t b f_t \frac{(1-\cos(2\phi))}{2} + k_{te} b \sin(\phi) - k_n b f_t \frac{\sin(2\phi)}{2} - k_{ne} b \cos(\phi) \tag{4.7.8}$$

To determine the mean cutting force per revolution, we must first augment the previous equations with the summation that accounts for all teeth on the cutter and the switching function that is nonzero only when the tooth angle is bounded by the cut start and exit angles.

$$F_x = \sum_{j=1}^{N_t} \left(k_t b f_t \frac{\sin(2\phi_j)}{2} + k_{te} b \cos(\phi_j) + k_n b f_t \frac{(1-\cos(2\phi_j))}{2} + k_{ne} b \sin(\phi_j) \right) g(\phi_j) \tag{4.7.9}$$

$$F_y = \sum_{j=1}^{N_t} \left(k_t b f_t \frac{(1-\cos(2\phi_j))}{2} + k_{te} b \sin(\phi_j) - k_n b f_t \frac{\sin(2\phi_j)}{2} - k_{ne} b \cos(\phi_j) \right) g(\phi_j) \tag{4.7.10}$$

$$F_z = \sum_{j=1}^{N_t} \left(-k_a b f_t \sin(\phi_j) - k_{ae} b \right) g(\phi_j) \tag{4.7.11}$$

The mean force per revolution in the x direction, for example, is then determined by $\bar{F}_x = \frac{1}{2\pi} \int_{\phi_s}^{\phi_e} F_x d\phi$. Because the integration limits are set between the start and exit angles, the switching function is always equal to one and is effectively removed from the integral. Also, the summation is incorporated by the multiplication of the integral by N_t as shown in Eq. 4.7.12. This equation is rewritten in Eq. 4.7.13.

$$\bar{F}_x = \frac{N_t}{2\pi}\int_{\phi_s}^{\phi_e}\left(k_t b f_t \frac{\sin(2\phi)}{2} + k_{te} b \cos(\phi) + k_n b f_t \frac{(1-\cos(2\phi))}{2} + k_{ne} b \sin(\phi)\right) d\phi \tag{4.7.12}$$

$$\bar{F}_x = \frac{N_t b}{4\pi}\int_{\phi_s}^{\phi_e} (k_t f_t \sin(2\phi) + 2k_{te}\cos(\phi) + k_n f_t - k_n f_t \cos(2\phi) + 2k_{ne}\sin(\phi)) d\phi \tag{4.7.13}$$

By application of $\int \sin(ax)dx = -\frac{1}{a}\cos(ax)$ and $\int \cos(ax)dx = \frac{1}{a}\sin(ax)$, the integral in Eq. 4.7.13 is determined to be:

$$\bar{F}_x = \frac{N_t b}{4\pi}\left[-\frac{k_t}{2} f_t \cos(2\phi) + 2k_{te}\sin(\phi) + k_n f_t \phi - \frac{k_n}{2} f_t \sin(2\phi) - 2k_{ne}\cos(\phi)\right]_{\phi_s}^{\phi_e}. \tag{4.7.14}$$

which can be rewritten as shown in Eq. 4.7.15.

$$\bar{F}_x = \left[\frac{N_t b f_t}{8\pi}(-k_t \cos(2\phi) + k_n(2\phi - \sin(2\phi))) + \frac{N_t b}{2\pi}(k_{te}\sin(\phi) - k_{ne}\cos(\phi))\right]_{\phi_s}^{\phi_e} \tag{4.7.15}$$

Similarly, the y and z direction mean cutting forces per revolution are:

$$\bar{F}_y = \left[\frac{N_t b f_t}{8\pi}(k_t(2\phi - \sin(2\phi)) + k_n \cos(2\phi)) - \frac{N_t b}{2\pi}(k_{te}\cos(\phi) + k_{ne}\sin(\phi))\right]_{\phi_s}^{\phi_e} \tag{4.7.16}$$

and

$$\bar{F}_z = \left[\frac{N_t b}{2\pi}(k_a f_t \cos(\phi) - k_{ae}\phi)\right]_{\phi_s}^{\phi_e}. \tag{4.7.17}$$

If we select 100% radial immersion (slotting) for the cutting tests, then $\phi_s = 0$ and $\phi_e = 180$ deg and Eqs. 4.7.15 through 4.7.17 simplify to:

$$\bar{F}_x = \frac{N_t b k_n}{4} f_t + \frac{N_t b k_{ne}}{\pi}, \tag{4.7.18}$$

$$\bar{F}_y = \frac{N_t b k_t}{4} f_t + \frac{N_t b k_{te}}{\pi}, \tag{4.7.19}$$

and

$$\bar{F}_z = -\frac{N_t b k_a}{\pi} f_t - \frac{N_t b k_{ae}}{2}. \tag{4.7.20}$$

4.7.2 Linear Regression

Given these expressions, we complete linear regressions (over chip thickness) to determine the six unknown cutting force coefficients: k_n, k_{ne}, k_t, k_{te}, k_a, and k_{ae} from measured (mean) force values. Note that the first term on the right hand side of the average force expressions in Eqs. 4.7.18 through 4.7.20 is a function of the feed per tooth, while the second term is not. These equations therefore match the (linear) slope-intercept form if f_t is the independent variable and the mean force is the dependent variable. In the x direction, for example, the slope is $\frac{N_t b k_n}{4}$ and the intercept is $\frac{N_t b k_{ne}}{\pi}$. See Fig. 4.7.1.

The form of the linear regression for the x direction is $\bar{F}_{x,i} = a_{0x} + a_{1x} f_{t,i} + E_i$, where $(f_{t,i}, \bar{F}_{x,i})$ are the data pairs, a_{0x} is the intercept, a_{1x} is the slope, and E_i is the error between the measured $\bar{F}_x$ values and the line $a_{0x} + a_{1x} f_t$. For $n > 2$ data pairs, the slope and intercept are determined by minimizing the sum of the errors squared [14].

$$\sum_{i=1}^{n} E_i^2 = \sum_{i=1}^{n} \left(\bar{F}_{x,i} - a_{0x} - a_{1x} f_{t,i}\right)^2$$

The slope and intercept expressions obtained from this minimization are provided in Eqs. 4.7.21 and 4.7.22.

$$a_{1x} = \frac{n \sum_{i=1}^{n} f_{t,i} \bar{F}_{x,i} - \sum_{i=1}^{n} f_{t,i} \sum_{i=1}^{n} \bar{F}_{x,i}}{n \sum_{i=1}^{n} f_{t,i}^2 - \left(\sum_{i=1}^{n} f_{t,i}\right)^2} \tag{4.7.21}$$

$$a_{0x} = \frac{1}{n} \sum_{i=1}^{n} \bar{F}_{x,i} - a_{1x} \frac{1}{n} \sum_{i=1}^{n} f_{t,i} \tag{4.7.22}$$

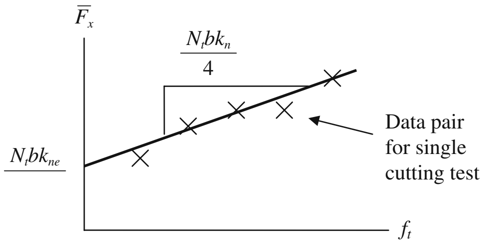

Fig. 4.7.1 Graph of Eq. 4.7.18, which relates the feed per tooth to the x direction mean force per revolution for slotting

To determine the quality of the linear fit to the data, we can calculate the coefficient of determination, r^2, where r is the correlation coefficient. The r^2 value describes how well the original uncertainty is explained by the linear model. For example, if $r^2 = 0.95$, then the line captures 95% of the data behavior. (There are exceptions where a high r^2 value does not guarantee a successful fit, but a visual analysis of the data and line is sufficient to identify these situations [14].) See Eq. 4.7.23, which is again specific to the x direction.

$$r_x^2 = \frac{\sum_{i=1}^{n}\left(\bar{F}_{x,i} - \frac{1}{n}\sum_{i=1}^{n}\bar{F}_{x,i}\right)^2 - \sum_{i=1}^{n}E_i^2}{\sum_{i=1}^{n}\left(\bar{F}_{x,i} - \frac{1}{n}\sum_{i=1}^{n}\bar{F}_{x,i}\right)^2} \tag{4.7.23}$$

Once the slope and intercept values are determined from the linear regressions for the x, y, and z direction mean force data (for slotting conditions), the cutting force coefficients are determined from Eqs. 4.7.24 through 4.7.26. In these expressions, the first a subscript denotes slope (1) or intercept (0), while the second subscript indicates the measurement direction (x, y, or z) as shown in Eqs. 4.7.21 and 4.7.22.

$$k_n = \frac{4a_{1x}}{N_t b} \quad k_{ne} = \frac{\pi \cdot a_{0x}}{N_t b} \tag{4.7.24}$$

$$k_t = \frac{4a_{1y}}{N_t b} \quad k_{te} = \frac{\pi \cdot a_{0y}}{N_t b} \tag{4.7.25}$$

$$k_a = -\frac{\pi \cdot a_{1z}}{N_t b} \quad k_{ae} = -\frac{2a_{0z}}{N_t b} \tag{4.7.26}$$

Example 4.7.1: Determination of cutting force coefficients To demonstrate the linear regression procedure for obtaining cutting force coefficient values from a particular tool-workpiece material pair, the MATLAB® program p_4_7_1_1.m is included on the companion CD. In this program, the cutting forces are first generated for the following conditions: $k_n = 190$ N/mm^2, $k_{ne} = 5$ N/mm, $k_t = 710$ N/mm^2, $k_{te} = 4$ N/mm, $k_a = 95$ N/mm^2, and $k_{ae} = 2$ N/mm; $b = 5$ mm, $f_t = \{0.05, 0.1, 0.15, 0.2, \text{and } 0.25\}$ mm/tooth, $\Omega = 5000$ rpm, $\phi_s = 0$, and $\phi_e = 180$ deg; and $N_t = 2$, $\beta = 30$ deg, and $d = 19$ mm for the square endmill. Figure 4.7.2 shows the forces for a single cutter revolution and feed per tooth of 0.25 mm, where (mean zero) Gaussian noise has been added. The mean forces for the x, y, and z directions are 136.1 N, 458.5 N, and −86.4 N, respectively. After the forces are generated and the mean values computed, the linear regression is completed to determine the slopes and intercepts for the x, y, and z directions; see Fig. 4.7.3. They are then used, together with the preselected N_t and b values, to determine the six cutting force coefficients as shown in

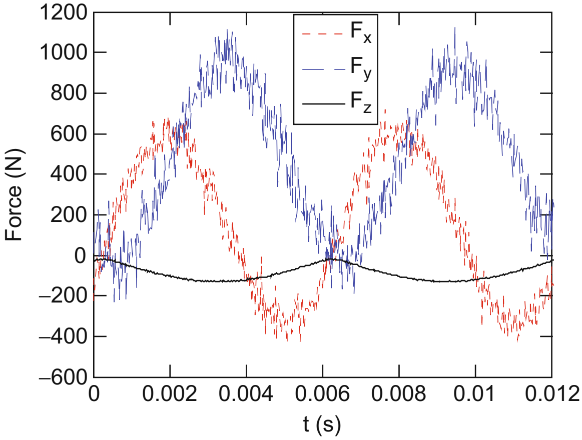

Fig. 4.7.2 Simulated cuttings forces for linear regression demonstration in EX. 4.7.1. The feed per tooth for the slotting cut is 0.25 mm/tooth

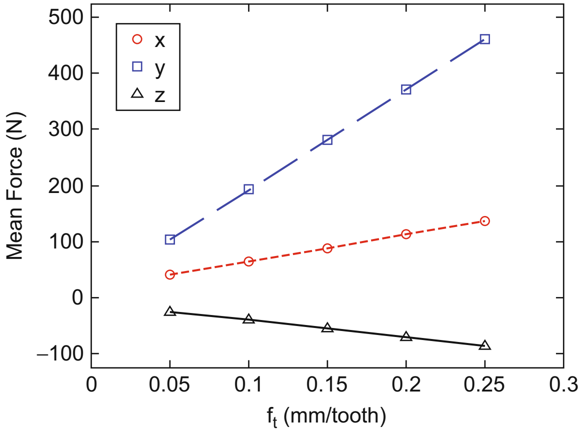

Fig. 4.7.3 Linear regression results for simulated forces in Ex. 4.7.1

Eqs. 4.7.24 through 4.7.26. Finally, the coefficients of determination are calculated.

4.7.3 Experimental Techniques

The required forces are typically measured using a table top cutting force dynamometer. The dynamometer is mounted to the machine table and aligned with the feed direction. Important considerations for force measurement include the force signal magnitudes and frequency content. As with any digital data collection, the range of the x, y, and z direction data acquisition channels should be selected so that adequate resolution is achieved. To set the maximum and minimum signal levels prior to machining, the simulation provided in p_4_7_1_1.m, for example, may be used with assumed coefficient values for the tool-workpiece material pair. Table 3.1.1 can be useful in estimating the cutting force coefficients.

Regarding frequency content, a dynamometer is also a dynamic system and therefore has its own associated frequency response. Naturally, if the cutting force has frequency content near a natural frequency of the dynamometer, then this content will be artificially amplified and the force data will be corrupted by the dynamometer dynamic response. The tooth passing frequency, defined in Eq. 4.1.14, provides a lower bound on the desired dynamometer bandwidth (i.e., the location of the first natural frequency for the dynamometer-workpiece combination). However, as shown in Fig. 4.1.15, multiple harmonics of the tooth passing frequency may be present, depending on the number of teeth and radial immersion. To determine the frequency response for a particular dynamometer-workpiece setup, impact testing can be applied. (It is necessary to include the mounted workpiece because it effectively mass loads the dynamometer and reduces it first natural frequency.) The impact hammer is used to excite the dynamometer in the x, y, and z directions and the corresponding force output is measured. The frequency-domain ratio of the output to input force can then be calculated and analyzed. To avoid data corruption by the dynamometer, the tooth passing frequency can be set such that there is no appreciable content at or beyond the first natural frequency of the dynamometer-workpiece combination. However, because decreases in cutting forces can be observed for higher cutting speeds [15], it may be preferable to test in the anticipated spindle speed range. In this case, one option is to filter the measured force using the inverse of the dynamometer force-to-input force frequency response. See, for example, the method proposed in [27]. An inverse filtering approach for a spindle-based torque dynamometer is also described in [28].

As a final note, it should of course be ensured that the cutting tests are stable. As described in the previous sections, the tool point frequency response function in the x and y directions should be measured and used as input, together with assumed cutting force coefficients, to one or both of the analytical stability lobe algorithms in order to estimate a stable axial depth of cut for the selected radial depth (slotting in Eqs. 4.7.24 through 4.7.26), number of cutter teeth, and spindle speed.

IN A NUTSHELL Of course, what constitutes “significant complexity” is in the eye of the beholder. Most of the information about stable and unstable cutting conditions can be correctly deduced using the approximation that the cutting force is proportional to the frontal area of the chip through a single cutting force coefficient. Increasing the accuracy of the prediction requires increasing the complexity of the model and the amount of required information. Knowing where to draw the line in order to obtain an answer that is good enough is the essence of engineering. Different readers will have varying objectives and will draw that line in different places.

Exercises

1. Compute the start and exit angles for the following milling cases.
   a) Up milling, 30% radial immersion
   b) Down milling, 40% radial immersion
2. Determine the tooth passing frequency for a cutter with three teeth rotating at 10000 rpm.
3. Calculate the maximum y direction force for a 40% radial immersion down milling cut carried out using a three tooth end mill; see Fig. e.4.3. The material-tool combination gives: $k_t = 720\,\text{N/mm}^2$ and $k_n = 200\ \text{N/mm}^2$ (aluminum alloy). Also, $b = 2.5$ mm and $f_t = 0.2$ mm/tooth. Assume a rigid cutting tool and workpiece.

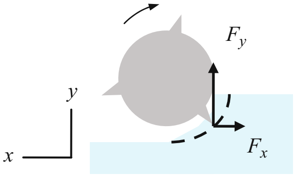

Fig. e.4.3 Down milling force geometry

4. For the average tooth angle milling stability analysis, complete parts a) through d). A 35% radial immersion up milling cut is to be performed using a square end mill with four teeth and the force angle, β, is 68 deg. See Fig. e.4.4.
   a) Determine the average angle of a tooth in the cut.
   b) Calculate the directional orientation factors.

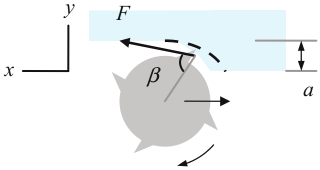

Fig. e.4.4 35% radial immersion up milling geometry

c) Compute the oriented frequency response function and identify the valid chatter frequency range(s) in Hz. The *x* direction dynamics are given by: $f_{nx} = 1000$ Hz, $k_x = 7 \times 10^6$ N/m, and $\zeta_x = 0.03$ and the *y* direction dynamics are: $f_{ny} = 1200$ Hz, $k_y = 6 \times 10^7$ N/m, and $\zeta_y = 0.04$. You may assume that these single degree of freedom parameters were obtained from a modal fit to frequency responses measured in the *x* and *y* directions with bandwidths of 0 to 2500 Hz.
d) Plot the first five stability lobes, $N = 0$ to 4. The workpiece material is 1020 carbon steel; see Table 3.1.1.

5. For the cut described in Exercise 4, use the Fourier approach to obtain the stability lobe diagram ($j = 0$ to 4).
6. Calculate the lowest axial depth for which a constant cutting force is obtained independent of the selected radial depth of cut. The helical square end mill has a diameter of 10 mm, six teeth, and a 42 deg helix angle.

References

1. Kumanchik, L. and Schmitz, T., 2007, Improved Analytical Chip Thickness Model for Milling, Precision Engineering, 31: 317–324.
2. Tlusty, J., W. Zaton, and F. Ismail, 1983, Stability Lobes in Milling, Annals of the CIRP, 32/1: 309–313.
3. Smith, S., and Tlusty, J., 1990, Update on High-Speed Milling Dynamics, Journal of Engineering for Industry, 112: 142–149.
4. Smith, S. and Tlusty, J., 1991, An Overview of Modeling and Simulation of the Milling Process, Journal of Engineering for Industry, 113: 169–175.
5. Altintas, Y. and Budak, E., 1995, Analytical Prediction of Stability Lobes in Milling, Annals of the CIRP, 44/1: 357–362.
6. Davies, M., Pratt, J., Dutterer, B., and Burns, T., 2000, The Stability of Low Radial Immersion Milling, Annals of the CIRP, 49/1: 37–40.
7. Davies, M., Pratt, J., Dutterer, B., and Burns, T., 2002, Stability Prediction for Low Radial Immersion Milling, Journal of Manufacturing Science and Engineering, 124/2: 217–225.
8. Bayly, P., Mann, B., Schmitz, T., Peters, D., Stépàn, G., Insperger, T., 2002, Effects of Radial Immersion and Cutting Direction on Chatter Instability in Endmilling, Proceedings of ASME International Mechanical Engineering Conference and Exposition, IMECE2002-34116, New Orleans, LA (on CD).
9. Mann, B., Bayly, P., Davies, M., and Halley, J., 2004, Limit Cycles, Bifurcations, and Accuracy of the Milling Process, Journal of Sound and Vibration, 227: 31–48.
10. Smith, S. and Tlusty, J., 1991, An Overview of Modeling and Simulation of the Milling Process, Journal of Engineering for Industry, 113: 169–175.
11. Tlusty, G., 2000, Manufacturing Equipment and Processes, Prentice-Hall, Upper Saddle River, NJ, Section 9.5.4.
12. Altintas, Y. and Lee, P., 1996, A General Mechanics and Dynamics Model for Helical End Mills, Annals of the CIRP, 45/1: 59–64.
13. Altintas, Y., 2000, Manufacturing Automation: Metal Cutting Mechanics, Machine Tool Vibrations, and CNC Design, Cambridge University Press, Cambridge, Section 2.8.1.
14. Chapra, S. and Canale, R., 1985, Numerical Methods for Engineers, McGraw-Hill Book Co., New York, NY, Section 10.1.

15. Duncan, G.S., 2006, Milling Dynamics Prediction and Uncertainty Analysis using Receptance Coupling Substructure Analysis, Ph.D. Dissertation, University of Florida, http://highspeedmachining.mae.ufl.edu/htmlsite/duncan_g.pdf.
16. Koenisgberger, F. and Sabberwal, A., 1961, An Investigation into the Cutting Force Pulsations during Milling Operations, International Journal of Machine Tool Design and Research, 1: 15–33.
17. Tlusty, J. and MacNeil, P., 1975, Dynamics of Cutting Forces in End Milling, Annals of the CIRP, 24/1: 21–25.
18. Kline, W., DeVor, R., and Lindberg, J., 1982, The Prediction of Cutting Forces in End Milling with Applications to Cornering Cuts, International Journal of Machine Tool Design and Research, 22: 7–22.
19. Fu, H., DeVor, R., and Kapoor, S., 1984, A Mechanistic Model for the Prediction of the Force System in Face Milling Operations, Journal of Engineering for Industry, 111: 27–36.
20. Yellowley, I., 1985, Observations of the Mean Values of Forces, Torque and Specific Power in the Peripheral Milling Process, International Journal of Machine Tool Design and Research, 25: 337–346.
21. Amarego, E. and Whitfield, R., 1985, Computer Based Modeling of Popular Machining Operations for Forces and Power Prediction, Annals of the CIRP, 34: 65–69.
22. Wang, J.-J., Liang, S., and Book, W., 1994, Convolution Analysis of Cutting Force Pulsation, Journal of Engineering for Industry, 116: 17–25.
23. Endres, W., DeVor, R., and Kapoor, S., 1995, A Dual-Mechanism Approach to the Prediction of Machining Forces, Part 1: Model Development, Journal of Engineering for Industry, 117: 526–533.
24. Budak, E., Altintas, Y., and Amarego, E., 1998, Prediction of Milling Force Coefficients from Orthogonal Cutting Data, Journal of Manufacturing Science and Engineering, 118: 216–224.
25. Jayaram, S., Kapoor, S., and DeVor, R., 2001, Estimation of the Specific Cutting Pressures for Mechanistic Cutting Force Models, International Journal of Machine Tools and Manufacture, 41: 265–281.
26. Wang, J.-J., and Zheng, C., 2002, An Analytical Force Model with Shearing and Ploughing Mechanisms for End Milling, International Journal of Machine Tools and Manufacture, 42: 761–771.
27. Jensen, S., Shin, Y., and Davies, P., 1996, Inverse Filtering of Unwanted System Dynamics in Cutting Force Measurement, Proceedings of the Dynamic Systems and Control Division, ASME International Mechanical Engineering Conference and Exposition, Atlanta, GA, pp. 167–174.
28. Smith, D., Smith, S., and Tlusty, J., 1998, High Performance Milling Torque Sensor, Journal of Manufacturing Science and Engineering, 120/3: 504–514.